

# Evolution of a Neutron Star From its Birth to Old Age

Madappa Prakash<sup>1</sup>, James M. Lattimer<sup>1</sup>, Jose A. Pons<sup>1</sup>, Andrew W. Steiner<sup>1</sup>,  
and Sanjay Reddy<sup>2</sup>

<sup>1</sup> Department of Physics & Astronomy,  
State University of New York at Stony Brook,  
Stony Brook, NY-11794-3800, USA

<sup>2</sup> Institute for Nuclear Theory,  
University of Washington,  
Seattle, WA 98195, USA

**Abstract.** The main stages in the evolution of a neutron star, from its birth as a proto-neutron star, to its old age as a cold, catalyzed configuration, are described. A proto-neutron star is formed in the aftermath of a successful supernova explosion and its evolution is dominated by neutrino diffusion. Its neutrino signal is a valuable diagnostic of its internal structure and composition. During its transformation from a hot, lepton-rich to a cold, catalyzed remnant, the possibility exists that it can collapse into a black hole, which abruptly terminates neutrino emissions. The essential microphysics, reviewed herein, that controls its evolution are the equation of state of dense matter and its associated neutrino opacities. Several simulations of the proto-neutron star evolution, involving different assumptions about the composition of dense matter, are described. After its evolution into a nearly isothermal neutron star a hundred or so years after its birth, it may be observable through its thermal emission in X-rays during its life in the next million years. Its surface temperature will depend upon the rapidity of neutrino emission processes in its core, which depends on the composition of dense matter and whether or not its constituents exhibit superfluidity and superconductivity. Observations of thermal emission offer the best hope of a determination of the radius of a neutron star. The implications for the underlying dense matter equation of state of an accurate radius determination are explored.

## 1 Introduction: The Tale

A proto-neutron star (PNS) is born in the aftermath of a successful supernova explosion as the stellar remnant becomes gravitationally decoupled from the expanding ejecta. Initially, the PNS is optically thick to neutrinos, that is, they are temporarily trapped within the star. The subsequent evolution of the PNS is dominated by  $\nu$ -diffusion which first results in deleptonization and subsequently in cooling. After a much longer time, photon emissions compete with neutrino emissions in neutron star cooling.

In this paper, we will focus upon the essential microphysical ingredients that govern the macrophysical evolution of neutron stars: the equation of state (EOS) of dense matter and its associated neutrino opacity. Among the characteristics of matter that widely vary among EOS models are their relative compressibilities

(important in determining a neutron star’s maximum mass), symmetry energies (important in determining the typical stellar radius and in the relative proton fraction) and specific heats (important in determining the local temperature). These characteristics play important roles in determining the matter’s composition, in particular the possible presence of additional components (such as hyperons, a pion or kaon condensate, or quark matter), and also significantly affect calculated neutrino opacities and diffusion time scales.

The evolution of a PNS proceeds through several distinct stages [1,2] and with various outcomes, as shown schematically in Fig. 1. Immediately following core bounce and the passage of a shock through the outer PNS’s mantle, the star contains an unshocked, low entropy core of mass  $M_c \simeq 0.7 M_\odot$  in which neutrinos are trapped (the first schematic illustration, labelled (1) in the figure). The core is surrounded by a low density, high entropy ( $5 < s < 10$ ) mantle that is both accreting matter from the outer iron core falling through the shock and also rapidly losing energy due to electron captures and thermal neutrino emission. The mantle extends up to the shock, which is temporarily stationary at a radius of about 200 km prior to an eventual explosion.

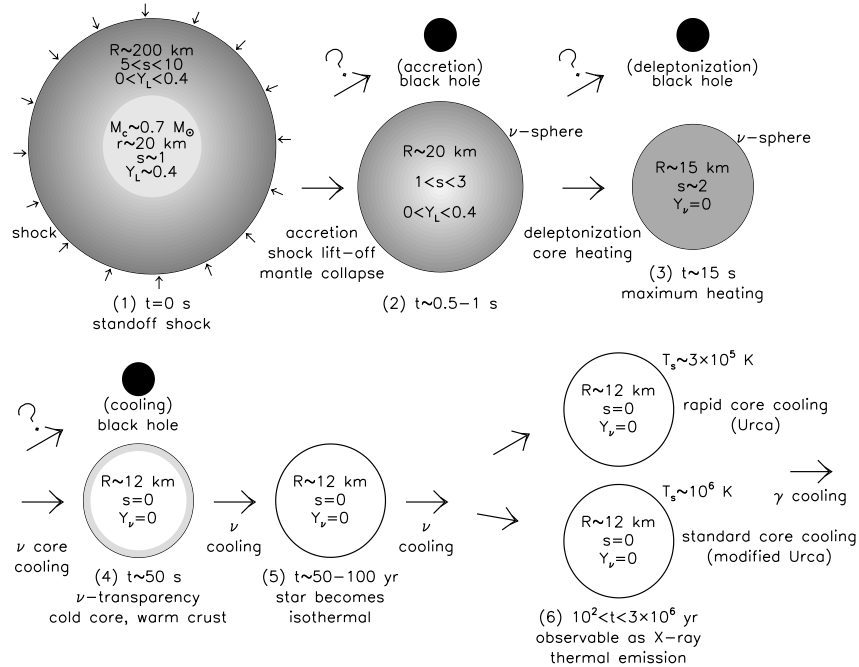


**Fig. 1.** The main stages of evolution of a neutron star. Shading indicates approximate relative temperatures.

After a few seconds (stage 2), accretion becomes less important if the supernova is successful and the shock lifts off the stellar envelope. Extensive neutrino

losses and deleptonization will have led to a loss of lepton pressure and the collapse of the mantle. If enough accretion occurs, however, the star's mass could increase beyond the maximum mass capable of being supported by the hot, lepton-rich matter. If this occurs, the remnant collapses to form a black hole and its neutrino emission is believed to quickly cease [3].

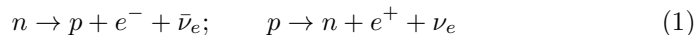
Neutrino diffusion deleptonizes the core on time scales of 10–15 s (stage 3). The diffusion of high-energy (200–300 MeV) neutrinos from the core to the surface where they escape as low-energy neutrinos (10–20 MeV) generates a large amount of heat within the star (a process akin to joule heating). The core's entropy approximately doubles, producing temperatures in the range of 30–60 MeV, during this time, even as neutrinos continue to be prodigiously emitted from the star's effective surface, known as the  $\nu$ -sphere.

Strange matter, in the form of hyperons, a Bose condensate, or quark matter, which is suppressed to extremely large densities when neutrinos are trapped in matter, could appear at the end of the deleptonization. The appearance of strange matter leads to a decrease in the theoretical maximum mass that matter is capable of supporting, leading to another possibility for black hole formation [4]. This would occur if the PNS's mass, which must be less than the maximum mass of hot, lepton-rich matter (or else a black hole would already have formed), is greater than the maximum mass of hot, lepton-poor matter. However, if strangeness does not appear, the theoretical maximum mass instead increases during deleptonization and the appearance of a black hole would be unlikely unless accretion in this stage remains significant.

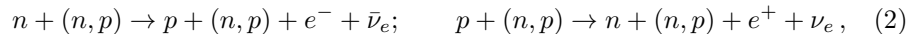
The PNS is now lepton-poor, but it is still hot. While the star has zero net neutrino number, thermally produced neutrino pairs of all flavors are abundant and dominate the emission. Neutrino diffusion continues to cool the star, but the average neutrino energy decreases, and the neutrino mean free path increases. After approximately 50 seconds (stage 4), the mean free path becomes comparable to the stellar radius, and the star finally becomes transparent to neutrinos. Since the threshold density for the appearance of strange matter decreases with decreasing temperature, a delayed collapse to a black hole is still possible during this epoch.

Neutrino observations from a galactic supernova will illuminate these stages. The observables will constrain time scales for deleptonization and cooling and the star's binding energy. Dimensionally, diffusion time scales are proportional to  $R^2(c\lambda)^{-1}$ , where  $R$  is the star's radius and  $\lambda$  is the effective neutrino mean free path. This generic relation illustrates how both the EOS and the composition, which determine both  $R$  and  $\lambda$ , influence evolutionary time scales. The total binding energy, which is primarily a function of stellar mass and radius (Lattimer & Prakash [5]), should be one of the most accurately measured quantities from neutrino observatories. Currently, Super-Kamiokande and SNO are capable of detecting thousands of neutrinos from a galactic supernova (distance less than 10 kpc). Exciting possibilities lie ahead with many other existing and planned new facilities [6].

Following the onset of neutrino transparency, the core continues to cool by neutrino emission, but the star's crust remains warm and cools less quickly. The crust is an insulating blanket which prevents the star from coming to complete thermal equilibrium and keeps the surface relatively warm ( $T \approx 3 \times 10^6$  K) for up to 100 years (stage 5). This timescale is primarily sensitive to the neutron star's radius and the thermal conductivity of the mantle [7], as can be noted from the approximate diffusive relationship  $\tau \propto \Delta R^2/\lambda$ , where  $\Delta R$  is the thickness of the crust. If the rapid decrease in the star's surface temperature predicted to occur when thermal equilibrium is ultimately achieved (see Fig. 16 in Section 6), a valuable constraint on the thickness of the crust, and hence the neutron star radius, could be obtained. The temperature of the surface after the interior of the star becomes isothermal (stage 6) is determined by the rate of neutrino emission in the star's core. The magnitude of the rate is primarily determined by the question of whether or not one or more of the so-called direct Urca processes can occur. The basic Urca process



operates even in degenerate matter because at finite temperature some of the nucleons are in excited states. In addition, direct Urca process involving hyperons, Bose condensates and quarks are also possible. In general, the direct Urca rate is proportional to  $T^4$ , and is so large that the surface temperatures fall to just a few times  $10^5$  K, which becomes very difficult to observe in X-rays except for very nearby stars. A relatively high surface temperature, closer to  $10^6$  K, will persist, however, if an Urca process can only occur indirectly with the participation of a spectator nucleon – the modified Urca process, which in the case of nucleons is



and leads to the so-called standard cooling scenario.

However, there are two circumstances that could prevent the direct Urca process from occurring. First, if the composition of the matter is such that the momentum triangle involving the non-neutrino particles cannot be closed, momentum conservation disallows this process. This occurs, in the case of  $n, p, e$ , for example, if the  $p$  and  $e^-$  abundances, which must be equal, are less than  $1/8$  the  $n$  abundance. This would be the case if the nuclear symmetry energy has a relatively weak density dependence. In addition, direct Urca processes involving hyperons, a Bose condensate, or quarks would not occur, of course, if they are not present. Second, direct Urca processes are suppressed if one of the reactants becomes superfluid. In this case, when the core temperature falls below the superfluid's critical temperature, the rapid cooling is terminated. In the case of a superfluid, the core cooling, and therefore the surface temperature, will be intermediate between those predicted by standard and rapid cooling models. Neutrino emission continues to dominate until neutron stars are approximately 1 million years old, at which point photon cooling from the surface begins to dominate. Unless the interiors cool very rapidly, X-ray emissions from stars remain relatively high until the photon cooling epoch.

Several neutron stars have been suggested to have observable thermal emissions in X-rays. In addition, the nearby neutron star RX J185635-3754, which is the closest known neutron star with a distance of approximately 60 pc, has detectable UV and optical thermal emissions as well. Such objects represent the best chance for measuring a neutron star's radius, especially if the redshift of spectral lines can be determined. Just-launched or proposed X-ray satellites, such as Chandra and XMM offer abundant prospects of observations of photon observations of neutron stars.

The organization of this article is as follows. Section 2 contains a summary of the basic equations of evolution for proto-neutron stars, including a discussion of the equilibrium diffusion approximation. Section 3 details the equation of state of dense matter, taking into account the possibility that neutrinos are trapped in the matter. The possibilities of hyperon-rich matter, kaon condensation and strange quark matter are also discussed here. In the event of a transition to matter containing kaons or quarks, we also consider the possibility that matter could be inhomogeneous with droplets of the strange matter embedded in normal matter. Neutrino-matter interactions are considered in Section 4, which includes discussions of the effects of composition, in-medium dispersion relations, and correlations, in both homogeneous and inhomogeneous phases. In Section 5, we present several simulations of the evolution of proto-neutron stars with different assumptions about the composition of dense matter and highlighting the role of the neutrino opacities. Focus is placed upon predicted neutrino signals and the differences anticipated for varying assumptions about the matter's composition. Section 6 describes the long-term cooling epoch, with a special emphasis on the role of direct Urca processes and superfluidity and a comparison with observations. A discussion of the possibility of detecting superfluidity, including quark color superfluidity, is included. In Section 7, the dependence of the structure of neutron stars on the underlying dense matter equation of state is explored. The relation between the matter's symmetry energy and the radii of neutron stars is highlighted. In addition, the moments of inertia and binding energies of neutron stars are discussed, and observational constraints on the mass and radius of the Vela pulsar from these considerations are elaborated. Section 8 contains our outlook.

## 2 Short-Term Neutrino Cooling: The First Minutes

The cooling of PNSs can be divided into two main regimes: the short-term, lasting perhaps one minute, during which the potential to observe the neutrino signal in terrestrial detectors exists, and the longer term period, lasting perhaps one million years, in which neutrino emissions dominate the cooling but the star is observable only through its thermal, photonic, emissions. This section summarizes the evolution equations relevant for the short-term Kelvin-Helmholtz phase and the estimation of its neutrino signature.

## 2.1 PNS Evolution Equations

The equations that govern the transport of energy and lepton number are obtained from the Boltzmann equation for massless particles [1,8,9,10]. We will focus on the non-magnetic, spherically symmetric situation. For the PNS problem, fluid velocities are small enough so that hydrostatic equilibrium is nearly fulfilled. Under these conditions, the neutrino transport equations in a stationary metric

$$ds^2 = -e^{2\phi} dt^2 + e^{2A} dr^2 + r^2 d\theta^2 + r^2 \sin^2 \theta d\Phi^2 \quad (3)$$

are:

$$\frac{\partial(N_\nu/n_B)}{\partial t} + \frac{\partial(e^\phi 4\pi r^2 F_\nu)}{\partial a} = e^\phi \frac{S_N}{n_B} \quad (4)$$

$$\frac{\partial(J_\nu/n_B)}{\partial t} + P_\nu \frac{\partial(1/n_B)}{\partial t} + e^{-\phi} \frac{\partial(e^{2\phi} 4\pi r^2 H_\nu)}{\partial a} = e^\phi \frac{S_E}{n_B}, \quad (5)$$

where  $n_B$  is the baryon number density and  $a$  is the enclosed baryon number inside a sphere of radius  $r$ . The quantities  $N_\nu$ ,  $F_\nu$ , and  $S_N$  are the number density, number flux and number source term, respectively, while  $J_\nu$ ,  $H_\nu$ ,  $P_\nu$ , and  $S_E$  are the neutrino energy density, energy flux, pressure, and the energy source term, respectively.

In the absence of accretion, the enclosed baryon number  $a$  is a convenient Lagrangian variable. The equations to be solved split naturally into a transport part, which has a strong time dependence, and a structure part, in which evolution is much slower. Explicitly, the structure equations are

$$\frac{\partial r}{\partial a} = \frac{1}{4\pi r^2 n_B e^A}, \quad \frac{\partial m}{\partial a} = \frac{\rho}{n_B e^A} \quad (6)$$

$$\frac{\partial \phi}{\partial a} = \frac{e^A}{4\pi r^4 n_B} (m + 4\pi r^3 P), \quad \frac{\partial P}{\partial a} = -(\rho + P) \frac{e^A}{4\pi r^4 n_B} (m + 4\pi r^3 P). \quad (7)$$

The quantities  $m$  (enclosed gravitational mass),  $\rho$  (mass-energy density), and  $P$  (pressure) include contributions from the leptons. To obtain the equations employed in the transport, Eq. (4) may be combined with the corresponding equation for the electron fraction

$$\frac{\partial Y_e}{\partial t} = -e^\phi \frac{S_N}{n_B} \quad (8)$$

to obtain

$$\frac{\partial Y_L}{\partial t} + e^{-\phi} \frac{\partial(e^\phi 4\pi r^2 F_\nu)}{\partial a} = 0. \quad (9)$$

Similarly, Eq. (5) may be combined with the matter energy equation

$$\frac{dU}{dt} + P \frac{d(1/n_B)}{dt} = -e^\phi \frac{S_E}{n_B}, \quad (10)$$

where  $U$  is the specific internal energy and use of the first law of thermodynamics yields

$$e^\phi T \frac{\partial s}{\partial t} + e^\phi \mu_\nu \frac{\partial Y_L}{\partial t} + e^{-\phi} \frac{\partial e^{2\phi} 4\pi r^2 H_\nu}{\partial a} = 0, \quad (11)$$

where  $s$  is the entropy per baryon.

## 2.2 The Equilibrium Diffusion Approximation

At high density and for temperatures above several MeV, the source terms in the Boltzmann equation are sufficiently strong to ensure that neutrinos are in thermal and chemical equilibrium with the ambient matter. Thus, the neutrino distribution function in these regions is both nearly Fermi-Dirac and isotropic. We can approximate the distribution function as an expansion in terms of Legendre polynomials to  $O(\mu)$ , which is known as the diffusion approximation. Explicitly,

$$f(\omega, \mu) = f_0(\omega) + \mu f_1(\omega), \quad f_0 = [1 + e^{(\frac{\omega - \mu_\nu}{kT})}]^{-1}, \quad (12)$$

where  $f_0$  is the Fermi-Dirac distribution function at equilibrium ( $T = T_{mat}$ ,  $\mu_\nu = \mu_\nu^{eq}$ ), with  $\omega$  and  $\mu_\nu$  being the neutrino energy and chemical potential, respectively. The main goal is to obtain a relation for  $f_1$  in terms of  $f_0$ . In the diffusion approximation, one obtains [10]

$$f_1 = -D(\omega) \left[ e^{-\Lambda} \frac{\partial f_0}{\partial r} - \omega e^{-\Lambda} \frac{\partial \phi}{\partial r} \frac{\partial f_0}{\partial \omega} \right]. \quad (13)$$

The explicit form of the diffusion coefficient  $D$  appearing above is given by

$$D(\omega) = \left( j + \frac{1}{\lambda_a} + \kappa_1^s \right)^{-1}. \quad (14)$$

The quantity  $j = j_a + j_s$ , where  $j_a$  is the emissivity and  $j_s$  is the scattering contribution to the source term. The absorptivity is denoted by  $\lambda_a$  and  $\kappa_1^s$  is the scattering contribution to the transport opacity. Substituting

$$\frac{\partial f_0}{\partial r} = - \left( T \frac{\partial \eta_\nu}{\partial r} + \frac{\omega}{T} \frac{\partial T}{\partial r} \right) \frac{\partial f_0}{\partial \omega}, \quad (15)$$

where  $\eta_\nu = \mu_\nu/T$  is the neutrino degeneracy parameter, in Eq. (13), we obtain

$$f_1 = -D(\omega) e^{-\Lambda} \left[ T \frac{\partial \eta}{\partial r} + \frac{\omega}{T e^\phi} \frac{\partial (T e^\phi)}{\partial r} \right] \left( - \frac{\partial f_0}{\partial \omega} \right). \quad (16)$$

Thus, the energy-integrated lepton and energy fluxes are

$$\begin{aligned} F_\nu &= - \frac{e^{-\Lambda} e^{-\phi} T^2}{6\pi^2} \left[ D_3 \frac{\partial (T e^\phi)}{\partial r} + (T e^\phi) D_2 \frac{\partial \eta}{\partial r} \right] \\ H_\nu &= - \frac{e^{-\Lambda} e^{-\phi} T^3}{6\pi^2} \left[ D_4 \frac{\partial (T e^\phi)}{\partial r} + (T e^\phi) D_3 \frac{\partial \eta}{\partial r} \right]. \end{aligned} \quad (17)$$

The coefficients  $D_2$ ,  $D_3$ , and  $D_4$  are related to the energy-dependent diffusion coefficient  $D(\omega)$  through

$$D_n = \int_0^\infty dx x^n D(\omega) f_0(\omega) (1 - f_0(\omega)) , \quad (18)$$

where  $x = \omega/T$ . These diffusion coefficients depend only on the microphysics of the neutrino-matter interactions (see §4 for details). The fluxes appearing in the above equations are for one particle species. To include all six neutrino types, we redefine the diffusion coefficients in Eq. (17):

$$D_2 = D_2^{\nu_e} + D_2^{\bar{\nu}_e} , \quad D_3 = D_3^{\nu_e} - D_3^{\bar{\nu}_e} , \quad D_4 = D_4^{\nu_e} + D_4^{\bar{\nu}_e} + 4D_4^{\nu_\mu} . \quad (19)$$

### 2.3 Neutrino Luminosities

A fair representation of the signal in a terrestrial detector can be found from the time dependence of the total neutrino luminosity and average neutrino energy together with an assumption of a Fermi-Dirac spectrum with zero chemical potential. We will return to discuss the improvements necessary to obtain more accurate information about the spectra.

The total neutrino luminosity is the time rate of change of the star's gravitational mass, and is therefore primarily a global property of the evolution. This luminosity, due to energy conservation, must also equal

$$L_\nu = e^{2\phi} 4\pi r^2 H_\nu \quad (20)$$

at the edge of the star. This relation serves as a test of energy conservation, at least for all times greater than about 5 ms, when the star comes into radiative equilibrium. For times greater than about 5 ms, initial transients become quite small and the predicted luminosities should be relatively accurate compared to full transport simulation. Estimate of the average energy of neutrinos is made from the temperature  $T_\nu$  of the matter at the neutrinosphere  $R_\nu$ , defined to be the location in the star where the flux factor  $\xi_H = 0.25$ . However, since the spectrum may not be Fermi-Dirac at the neutrinosphere, a diffusion scheme cannot give a very precise value for the average energy. We use the average energy  $\langle E_\nu \rangle \approx 3T_\nu$ , where  $T_\nu$  is a mass average in the outermost zone. Because it is a globally determined quantity, the luminosity  $L_\nu$  is necessarily more accurately determined than either  $R_\nu$  or  $T_\nu$ .

## 3 The Equation of State of Neutrino Trapped Matter

The rationale for considering different possibilities for the composition of dense matter is largely due to the fact that QCD at finite baryon density remains unsolved. Effective QCD based models have raised intriguing possibilities concerning the composition of dense matter including the presence of hyperons, pion or kaon condensates, and quark matter (see [4] for extensive references). It



is also important to have predictions for the plain-vanilla case of nucleons alone. The contrast can be dramatic, since additional components offer the possibility of BH formation during the evolution of a PNS. In what follows, the symbols  $np$  refer to matter with nucleons alone,  $npH$  to matter including hyperons,  $npK$  to matter with nucleons and kaons, and  $npQ$  to matter with nucleons and quarks. In all cases, leptons in beta equilibrium are included.

### 3.1 Matter with Nucleons and Hyperons

The masses and radii of neutron stars depend upon the matters' compressibility, the composition of matter at high density, and the nuclear symmetry energy (e.g., [4]). In the PNS problem, the finite temperature aspects of the EOS also play an important role. During the early evolution the entropy in the central regions is moderately high,  $s \sim 1 - 2$  (in units of Boltzmann's constant), which correspond to temperatures in the range  $T = 20 - 50$  MeV. These features may be explored by employing a finite temperature field-theoretical model in which the interactions between baryons are mediated by the exchange of  $\sigma, \omega$ , and  $\rho$  mesons<sup>1</sup>. The hadronic Lagrangian density is given by [12]

$$\begin{aligned}
 L_H = & \sum_i \overline{B}_i (-i\gamma^\mu \partial_\mu - g_{\omega i} \gamma^\mu \omega_\mu - g_{\rho i} \gamma^\mu \mathbf{b}_\mu \cdot \mathbf{t} - M_i + g_{\sigma i} \sigma) B_i \\
 & - \frac{1}{4} W_{\mu\nu} W^{\mu\nu} + \frac{1}{2} m_\omega^2 \omega_\mu \omega^\mu - \frac{1}{4} \mathbf{B}_{\mu\nu} \mathbf{B}^{\mu\nu} + \frac{1}{2} m_\rho^2 b_\mu b^\mu \\
 & + \frac{1}{2} \partial_\mu \sigma \partial^\mu \sigma - \frac{1}{2} m_\sigma^2 \sigma^2 - U(\sigma)
 \end{aligned} \tag{21}$$

Here,  $B$  are the Dirac spinors for baryons and  $\mathbf{t}$  is the isospin operator. The sums include baryons  $i = n, p, \Lambda, \Sigma$ , and  $\Xi$ . The field strength tensors for the  $\omega$  and  $\rho$  mesons are  $W_{\mu\nu} = \partial_\mu \omega_\nu - \partial_\nu \omega_\mu$  and  $\mathbf{B}_{\mu\nu} = \partial_\mu \mathbf{b}_\nu - \partial_\nu \mathbf{b}_\mu$ , respectively. The potential  $U(\sigma)$  represents the self-interactions of the scalar field and is taken to be of the form [13]

$$U(\sigma) = \frac{1}{3} b M_n (g_{\sigma N} \sigma)^3 + \frac{1}{4} c (g_{\sigma N} \sigma)^4. \tag{22}$$

The partition function  $Z_H$  for the hadronic degrees of freedom is evaluated in the mean field approximation. The total partition function  $Z_{total} = Z_H Z_L$ , where  $Z_L$  is the standard noninteracting partition function of the leptons. Using  $Z_{total}$ , the thermodynamic quantities can be obtained in the standard way. The additional conditions needed to obtain a solution are provided by the charge neutrality

<sup>1</sup> Note that the couplings in these models may be chosen to reproduce the results of numerically more intensive microscopic potential models, such as that of Akmal and Pandharipande [11], so that the gross features of the zero temperature thermodynamics can be reproduced. Additional advantages to this approach are that the effects of finite temperature and arbitrary proton fraction may be incorporated more easily.

requirement, and, when neutrinos are trapped, the set of equilibrium chemical potential relations required by the general condition

$$\mu_i = b_i \mu_n - q_i (\mu_l - \mu_{\nu_l}). \quad (23)$$

where  $b_i$  is the baryon number of particle  $i$  and  $q_i$  is its charge. The introduction of additional variables, the neutrino chemical potentials, requires additional constraints, which we supply by fixing the lepton fractions,  $Y_{L\ell}$ , appropriate for conditions prevailing in the evolution of the PNS. In addition to models containing only nucleonic degrees of freedom (GM1np & GM3np) we investigate models that allow for the presence of hyperons (GM1npH & GM3npH). For the determination of the various coupling constants appearing in  $Z_H$  see [4].

The lepton chemical potentials influence the deleptonization epoch. For np models a lower nuclear symmetry energy favors a larger  $\nu_e$  fraction and has little effect on the  $e^-$  fraction at  $Y_L = 0.4$ . Models with hyperons lead to significantly larger  $\mu_{\nu_e}$  and lower  $\mu_e$ , both of which influence the diffusion of electron neutrinos. The electron chemical potentials in neutrino free matter are reduced to a greater extent by changes in composition and symmetry energy as there are no neutrinos to compensate for changes in  $\hat{\mu} = \mu_n - \mu_p$ .

### 3.2 Matter with a Kaon Condensate

The contents of this section are extracted from Pons et al. [14]. For the kaon sector, we use a Lagrangian that contains the usual kinetic energy and mass terms along with the meson interactions [15]. Kaons are coupled to the meson fields through minimal coupling; specifically,

$$L_K = \mathcal{D}_\mu^* K^+ \mathcal{D}^\mu K^- - m_K^{*2} K^+ K^-, \quad (24)$$

where the vector fields are coupled via the standard form

$$\mathcal{D}_\mu = \partial_\mu + ig_{\omega K} \omega_\mu + ig_{\rho K} \gamma^\mu \mathbf{b}_\mu \cdot \mathbf{t} \quad (25)$$

and  $m_K^* = m_K - \frac{1}{2} g_{\sigma K} \sigma$  is the effective kaon mass.

In the mean field approach, the thermodynamic potential per unit volume in the kaon sector is [14]

$$\begin{aligned} \frac{\Omega_K}{V} &= \frac{1}{2} (f\theta)^2 (m_K^{*2} - (\mu + X_0)^2) \\ &+ T \int_0^\infty \frac{d^3 p}{(2\pi)^3} \left[ \ln(1 - e^{-\beta(\omega^- - \mu)}) + \ln(1 - e^{-\beta(\omega^+ + \mu)}) \right], \end{aligned} \quad (26)$$

where  $X_0 = g_{\omega K} \omega_0 + g_{\rho K} b_0$ , the Bose occupation probability

$f_B(x) = (e^{\beta x} - 1)^{-1}$ ,  $\omega^\pm = \sqrt{p^2 + m_K^{*2}} \pm X_0$ ,  $f = 93$  MeV is the pion decay constant and the condensate amplitude,  $\theta$ , can be found by extremization of

the partition function. This yields the solution  $\theta = 0$  (no condensate) or, if a condensate exists, the equation

$$m_K^* = \mu_K + X_0 \quad (27)$$

where  $\mu_K$  is the kaon chemical potential. In beta-stable stellar matter the conditions of charge neutrality

$$\sum_B q_B n_B - n_e - n_K = 0 \quad (28)$$

and chemical equilibrium

$$\mu_i = b_i \mu_n - q_i (\mu_l - \mu_{\nu_\ell}) \quad (29)$$

$$\mu_K = \mu_n - \mu_p \quad (30)$$

are also fulfilled.

The kaon condensate is assumed to appear by forming a mixed phase with the baryons satisfying Gibbs' rules for phase equilibrium [16]. Matter in this mixed phase is in mechanical, thermal and chemical equilibrium, so that

$$p^I = p^{II}, \quad T^I = T^{II}, \quad \mu_i^I = \mu_i^{II}, \quad (31)$$

where the superscripts I and II denote the nucleon and kaon condensate phases, respectively. The conditions of global charge neutrality and baryon number conservation are imposed through the relations

$$\begin{aligned} \chi q^I + (1 - \chi) q^{II} &= 0 \\ \chi n_B^I + (1 - \chi) n_B^{II} &= n_B, \end{aligned} \quad (32)$$

where  $\chi$  denotes the volume fraction of nucleonic phase,  $q$  the charge density, and  $n_B$  the baryon density. We ignore the fact that the phase with the smallest volume fraction forms finite-size droplets; in general, this would tend to decrease the extent of the mixed phase region. Further general consequences of imposing Gibbs' rules in a multicomponent system are that the pressure varies continuously with density in the mixed phase and that the charge densities must have opposite signs in the two phases to satisfy global charge neutrality. We note, however, that not all choices of nucleon-nucleon and kaon-nucleon interactions permit the Gibbs' rules to be satisfied (for an example of such an exception, see [14]). The models chosen in this work *do* allow the Gibbs' rules to be fulfilled at zero and finite temperatures and in the presence of trapped neutrinos.

The nucleon-meson couplings are determined by adjusting them to reproduce the properties of equilibrium nucleonic matter at  $T = 0$ . We use the numerical values used by [13], i.e., equilibrium density  $n_0 = 0.153 \text{ fm}^{-3}$ , equilibrium energy per particle of symmetric nuclear  $E/A = -16.3 \text{ MeV}$ , effective mass  $M^* = 0.78M$ , compression modulus  $K_0 = 240 \text{ MeV}$ , and symmetry energy  $a_{sym} = 32.5 \text{ MeV}$ . These values yield the coupling constants  $g_\sigma/m_\sigma = 3.1507 \text{ fm}$ ,  $g_\omega/m_\omega = 2.1954 \text{ fm}$ ,  $g_\rho/m_\rho = 2.1888$ ,  $b = 0.008659$ , and  $c = -0.002421$ .

The kaon-meson couplings  $g_{\sigma K}$  and  $g_{\omega K}$  are related to the magnitude of the kaon optical potential  $U_K$  at the saturation density  $n_0$  of isospin symmetric nuclear matter:

$$U_K(n_0) = -g_{\sigma K}\sigma(n_0) - g_{\omega K}\omega_0(n_0). \quad (33)$$

Fits to kaonic atom data have yielded values in the range  $-(50 - 200)$  MeV [17,18,19,20,21]. We use  $g_{\omega K} = g_{\omega N}/3$  and  $g_{\rho K} = g_{\rho N}/2$  on the basis of simple quark and isospin counting. Given the uncertainty in the magnitude of  $|U_K|$ , consequences for several values of  $|U_K|$  were explored in [14]. Moderate values of  $|U_K|$  generally produce a second order phase transition and, therefore, lead to moderate effects on the gross properties of stellar structure. Values in excess of 100 MeV were found necessary for a first order phase transition to occur; in this case kaon condensation occurs at a relatively low density with an extended mixed phase region, which leads to more pronounced effects on the structure due to a significant softening of the EOS.

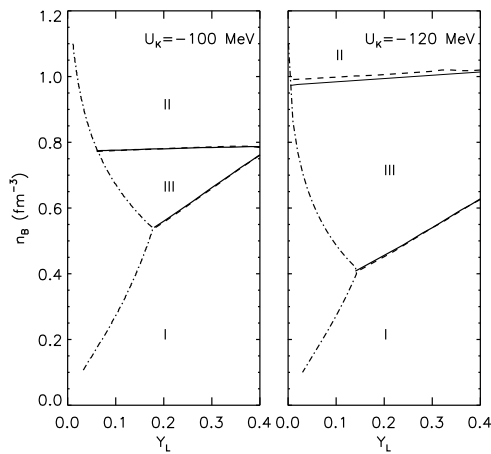


**Fig. 2.** Phase boundaries between pure nucleonic matter (I), pure kaon condensed matter (II) and a mixed phase (III) in the  $Y_L$ - $n_B$  plane for  $U_K = -100$  MeV (left panel) and  $U_K = -120$  MeV (right panel). The solid line corresponds to  $s = 0$  and the dashed line to  $s = 1$ . The dashed-dotted line shows the baryon density as a function of the lepton fraction for  $s = 0$ , neutrino-free ( $Y_L = Y_e$ ) matter

The phase boundaries of the different phases are displayed in Fig. 2 in a  $Y_L$ - $n_B$  plane for an optical potential  $U_K$  of  $-100$  MeV (left) and  $-120$  MeV (right), respectively. The nucleonic phase, the pure kaon matter phase, and the mixed phase are labelled I, II, and III, respectively. Solid lines mark the phase transition at zero temperature and dashed lines mark the phase transition at an entropy per baryon of  $s = 1$ . Note that finite entropy effects are small and do not affect significantly the phase transition density. The dash-dotted line shows the electron fraction  $Y_e$  as a function of density in cold, catalyzed matter (for

which  $Y_L = Y_e$ ), which is the final evolutionary state. The region to the left of this line corresponds to negative neutrino chemical potentials and cannot be reached during normal evolutions. The solid and dashed lines, which separate the pure phases from the mixed phase, vary roughly linearly with the lepton fraction. Also notice the large, and nearly constant, densities of the boundary between the mixed phase III and the pure kaon phase II. These densities, for the cases shown, lie above the central densities of the maximum mass stars, so that region II does not generally exist in proto-neutron stars (see [14]). The effect of increasing the lepton number is to reduce the size of the mixed phase (which in fact shrinks to become a second order phase transition for  $Y_L > 0.4$  and  $U_K = -100$  MeV) and to shift the critical density to higher densities. A similar effect is produced by decreasing the magnitude of the optical potential.

### 3.3 Matter with Quarks

The discussion in this section follows the work of Steiner, Prakash & Lattimer [22]. The thermodynamic potential of the quark phase is  $\Omega = \Omega_{\text{FG}} + \Omega_{\text{Int}}$ , where

$$\frac{\Omega_{\text{FG}}}{V} = 2N_c T \sum_{i=u,d,s} \int \frac{d^3p}{(2\pi)^3} [\ln(1 - f_i) + \ln(1 - \bar{f}_i)] \quad (34)$$

denotes the Fermi gas contribution arising from quarks. We consider three flavors,  $i = u, d, s$  and three colors,  $N_c = 3$  of quarks. The distribution functions of fermions and anti-fermions are  $f_i = [1 + \exp(\beta(E_i - \mu_i))]^{-1}$  and  $\bar{f}_i = [1 + \exp(\beta(E_i + \mu_i))]^{-1}$ , where  $E_i$  and  $\mu_i$  are the single particle energy and chemical potential, respectively, of quark species  $i$ . To explore the sensitivity of the quark model, we contrast the results of the MIT bag and the Nambu Jona-Lasinio (henceforth NJL) models for  $\Omega_{\text{Int}}$ .

In the MIT bag model, the Fermi gas contribution is calculated using current, as opposed to dynamical, quark masses. We will restrict ourselves to the simplest bag model and keep only the constant cavity pressure term. The results are qualitatively similar to what is obtained by including perturbative corrections, if the bag constant  $B$  is slightly altered [23].

Several features of the Lagrangian of Quantum Chromo-Dynamics (QCD), including the spontaneous breakdown of chiral symmetry, are exhibited by the Nambu Jona-Lasinio (NJL) model, which shares many symmetries with QCD. In its commonly used form, the NJL Lagrangian reads

$$\begin{aligned} \mathcal{L} = & \bar{q}(i\cancel{\partial} - \hat{m}_0)q + G \sum_{k=0}^8 [(\bar{q}\lambda_k q)^2 + (\bar{q}i\gamma_5\lambda_k q)^2] \\ & - K [\det_f(\bar{q}(1 + \gamma_5)q) + \det_f(\bar{q}(1 - \gamma_5)q)]. \end{aligned} \quad (35)$$

The determinant operates over flavor space,  $\hat{m}_0$  is the  $3 \times 3$  diagonal current quark mass matrix,  $\lambda_k$  represents the 8 generators of SU(3), and  $\lambda_0$  is proportional to the identity matrix. The four-fermion interactions stem from the

original formulation of this model [24], while the flavor mixing, determinantal interaction is added to break  $U_A(1)$  symmetry [25]. Since the coupling constants  $G$  and  $K$  are dimensionful, the quantum theory is non-renormalizable. Therefore, an ultraviolet cutoff  $\Lambda$  is imposed, and results are considered meaningful only if the quark Fermi momenta are well below this cutoff. The coupling constants  $G$  and  $K$ , the strange quark mass  $m_{s,0}$ , and the three-momentum ultraviolet cutoff parameter  $\Lambda$ , are fixed by fitting the experimental values of  $f_\pi$ ,  $m_\pi$ ,  $m_K$  and  $m_\eta$ . We use the values of Ref. [26], namely  $\Lambda = 602.3$  MeV,  $G\Lambda^2 = 1.835$ ,  $K\Lambda^5 = 12.36$ , and  $m_{0,s} = 140.7$  MeV, obtained using  $m_{0,u} = m_{0,d} = 5.5$  MeV. The subscript “0” denotes current quark masses. Results of the gross properties of PNSs obtained by the alternative parameter sets of Refs. [27] and [28] are similar to the results quoted below.

In the mean field approximation at finite temperature and at finite baryon density, the thermodynamic potential due to interactions among quarks is given by [28]:

$$\begin{aligned} \frac{\Omega_{\text{Int}}}{V} = & -2N_c \sum_{i=u,d,s} \int \frac{d^3p}{(2\pi)^3} \left( \sqrt{m_i^2 + p^2} - \sqrt{m_{0,i}^2 + p^2} \right) \\ & + 2G \langle \bar{q}_i q_i \rangle^2 - 4K \langle \bar{q}_u q_u \rangle \langle \bar{q}_d q_d \rangle \langle \bar{q}_s q_s \rangle. \end{aligned} \quad (36)$$

In both Eqs. (34) and (36) for the NJL model, the quark masses are dynamically generated as solutions of the gap equation obtained by requiring that the potential be stationary with respect to variations in the quark condensate  $\langle \bar{q}_i q_i \rangle$ :

$$m_i = m_{0,i} - 4G \langle \bar{q}_i q_i \rangle + 2K \langle \bar{q}_j q_j \rangle \langle \bar{q}_k q_k \rangle, \quad (37)$$

( $q_i, q_j, q_k$ ) representing any permutation of ( $u, d, s$ ). The quark condensate  $\langle \bar{q}_i q_i \rangle$  and the quark number density  $n_i = \langle q_i^\dagger q_i \rangle$  are given by:

$$\begin{aligned} \langle \bar{q}_i q_i \rangle &= -2N_c \int \frac{d^3p}{(2\pi)^3} \frac{m_i}{E_i} [1 - f_i - \bar{f}_i] \\ n_i = \langle q_i^\dagger q_i \rangle &= 2N_c \int \frac{d^3p}{(2\pi)^3} [f_i - \bar{f}_i]. \end{aligned} \quad (38)$$

A comparison between the MIT bag and NJL models is facilitated by defining an effective bag pressure in the NJL model to be [29]  $B_{eff} = \Omega_{\text{int}}/V - B_0$  with  $B_0 V = \Omega_{\text{int}}|_{n_u=n_d=n_s=0}$  a constant value which makes the vacuum energy density zero. In this way, the thermodynamic potential can be expressed as  $\Omega = B_{eff}V + \Omega_{FG}$  which is to be compared to the MIT bag result  $\Omega = BV + \Omega_{FG}$ . Note, however, that  $\Omega_{FG}$  in the NJL model is calculated using the dynamical quark masses from Eq. (37).

The temperature as a function of baryon density for fixed entropy and net lepton concentration is presented in Fig. 3, which compares the cases ( $s = 1, Y_{L_e} = 0.4$ ) and ( $s = 2, Y_{\nu_e} = 0$ ) both including and ignoring quarks. The temperature for a multicomponent system in a pure phase can be analyzed with the relation

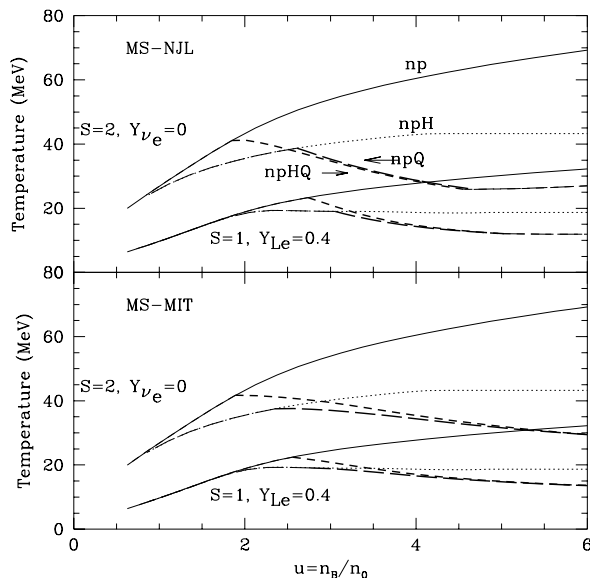


**Fig. 3.** Temperature versus density in units of  $n_0$  for two PNS evolutionary snapshots. The upper (lower) panel displays results for the NJL (MIT bag) Lagrangian. The parameters  $\zeta = \xi = 0$  in the Müller-Serot (MS) hadronic Lagrangian [30] are chosen. Results are compared for matter containing only nucleons (np), nucleons plus hyperons (npH), nucleons plus quarks (npQ) and nucleons, hyperons and quarks (npHQ). Bold curves indicate the mixed phase region

for degenerate Fermi particles

$$T = \frac{s}{\pi^2} \left( \frac{\sum_i p_{F_i} \sqrt{p_{F_i}^2 + (m_i^*)^2}}{\sum_i p_{F_i}^3} \right)^{-1}, \quad (39)$$

where  $m_i^*$  and  $p_{F_i}$  are the effective mass and the Fermi momentum of component  $i$ , respectively. This formula is quite accurate since the hadron and quark Fermi energies are large compared to the temperature. The introduction of hyperons or quarks lowers the Fermi energies of the nucleons and simultaneously increases the specific heat of the matter, simply because there are more components. In the case of quarks, a further increase, which is just as significant, occurs due to the fact that quarks are rather more relativistic than hadrons. The combined effects for quarks are so large that, in the case  $M_0^* = 0.6M$  shown in Fig. 3, an actual reduction of temperature with increasing density occurs along an adiabat. The effect is not necessarily as dramatic for other choices of  $M_0^*$ , but nevertheless indicates that the temperature will be smaller in a PNS containing quarks than in stars without quarks. The large reduction in temperature might also influence neutrino opacities, which are generally proportional to  $T^2$ . However, the presence

of droplet-like structures in the mixed phase, not considered here, will modify the specific heat. In addition, these structures may dominate the opacity in the mixed phase [31]. However, a PNS simulation is necessary to consistently evaluate the thermal evolution, since the smaller pressure of quark-containing matter would tend to increase the star's density and would oppose this effect.

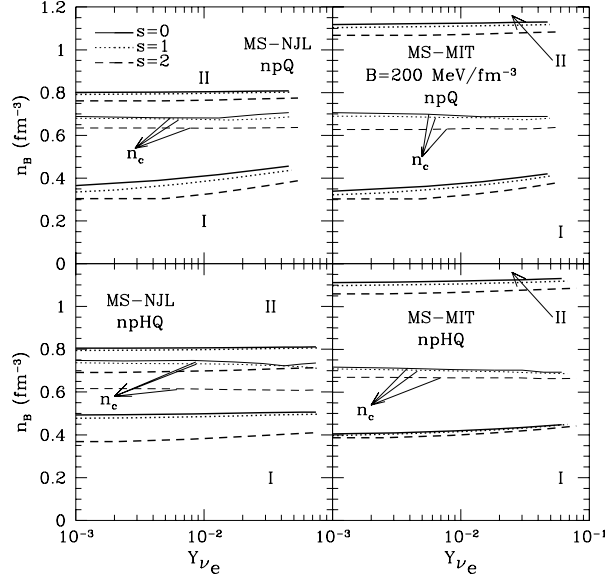


**Fig. 4.** The phase diagram of the quark-hadron transition in the baryon number density - neutrino concentration plane for three representative snapshots during the evolution of a proto-neutron star. The left (right) panels are for the NJL (MIT bag) quark EOS, and hyperons are (are not) included in the bottom (top) panels. The parameters  $\zeta = \xi = 0$  in the Müller-Serot (MS) hadronic Lagrangian are chosen. The lower- and upper-density boundaries of the mixed phase are indicated by bold curves. The central densities of maximum mass configurations are shown by thin curves

This last point is highlighted in Fig. 4 which shows phase diagrams for the mixed phase in the baryon density-neutrino fraction plane. The upper and lower boundaries of the mixed phase region are displayed as bold lines, while the central densities of the maximum mass configurations are shown as light lines. In no case, for either quark model and whether or not hyperons are included, are pure quark stars possible. The high-density phase boundaries are always well above the central densities. While in the optimum case, in which the parameters of both the hadronic and quark EOSs are fine-tuned, it is possible for a pure quark core to form if  $B < 150 \text{ MeV fm}^{-3}$ , the maximum mass decreases below  $1.44 M_{\odot}$  if  $B < 145 \text{ MeV fm}^{-3}$ . This narrow window, which further decreases or



disappears completely if the hadronic EOS is altered, suggests that pure quark configurations may be unlikely.

### 3.4 Inhomogeneous Phases

It is widely believed that some type of phase transition will occur in nuclear matter at high densities. For example, a transition to deconfined quark matter should exist at sufficiently high density, and at lower densities, a first-order transition to a Bose condensate phase might exist. Such phase transitions are expected to soften the equation of state, leading to changes in the mass-radius relation and lowering the maximum mass. Phase transitions can also influence transport and weak interaction rates in matter.

Glendenning has shown that, due to the existence of two conserved charges (baryon number and charge) instead of just one, first order phase transitions can lead to a large mixed phase region in the neutron star interior [32]. The mixed phase consists of high baryon density, negatively charged, matter coexisting with lower density, positively charged, baryonic matter. The situation is entirely analogous to the well-known situation involving the mixed phase consisting of nuclei and a surrounding nucleonic vapor that occurs below nuclear saturation density [33]. The occurrence of a mixed phase, as opposed to a Maxwell construction, results in a wider transition in which bulk thermodynamic properties such as pressure vary less rapidly but are softer over a wider density range. In addition, the propagation of neutrinos whose wavelength is greater than the typical droplet size and less than the inter-droplet spacing will be greatly affected by the heterogeneity of the mixed phase, as a consequence of the coherent scattering of neutrinos from the matter in the droplet. The thermodynamics and the effect on neutron star structure of two situations have been studied in some detail: first order kaon condensation [15,34,35] and the quark-hadron transition [36,37].

## 4 Neutrino-Matter Interaction Rates

One of the important microphysical inputs in PNS simulations is the neutrino opacity at supra-nuclear density [1,38,39,40,41,42] Although it was realized over a decade ago that the effects due to degeneracy and strong interactions significantly alter the neutrino mean free paths, it is only recently that detailed calculations have become available [31,43,44,45,46,47,48,49]. The scattering and absorption reactions that contribute to the neutrino opacity are

$$\nu_e + B \rightarrow e^- + B', \quad \bar{\nu}_e + B \rightarrow e^+ + B', \quad (40)$$

$$\nu_X + B \rightarrow \nu_X + B', \quad \nu_X + e^- \rightarrow \nu_X + e^-, \quad (41)$$

where the scattering reactions are common to all neutrino species and the dominant source of opacity for the electron neutrinos is due to the charged reaction. The weak interaction rates in hot and dense matter are modified due to many in-medium effects. The most important of these are:

(1) *Composition*: The neutrino mean free paths depend sensitively on the composition which is sensitive to the nature of strong interactions. First, the different degeneracies of the different Fermions determines the single-pair response due to Pauli blocking. Second, neutrinos couple differently to different baryonic species; consequently, the net rates will depend on the individual concentrations.

(2) *In-medium dispersion relations*: At high density, the single-particle spectra are significantly modified from their noninteracting forms due to effects of strong interactions. Interacting matter features smaller effective baryon masses and energy shifts relative to non-interacting matter.

(3) *Correlations*: Repulsive particle-hole interactions and Coulomb interactions generally result in a screened dielectric response and also lead to collective excitations in matter. These effects may be calculated using the Random Phase Approximation (RPA), in which ring diagrams are summed to all orders. Model calculations [43,45,47,50,51,52,53,54,55] indicate that at high density the neutrino cross sections are suppressed relative to the case in which these effects are ignored. In addition, these correlations enhance the average energy transfer in neutrino-nucleon collisions. Improvements in determining the many-body dynamic form factor and assessing the role of particle-particle interactions in dense matter at finite temperature are necessary before the full effects of many-body correlations may be ascertained.

The relative importance of the various effects described above on neutrino transport is only beginning to be studied systematically. As a first step, we will focus on effects due to modifications (1) through (3) above. To see how this is accomplished, we start with a general expression for the differential cross section [56,57]

$$\frac{1}{V} \frac{d^3\sigma}{d^2\Omega_3 dE_3} = -\frac{G_F^2 E_3}{128\pi^2 E_1} \left[ 1 - \exp\left(\frac{-q_0 - (\mu_2 - \mu_4)}{T}\right) \right]^{-1} \times (1 - f_3(E_3)) \text{Im} (L^{\alpha\beta} \Pi_{\alpha\beta}^R), \quad (42)$$

where the incoming neutrino energy is  $E_1$  and the outgoing electron energy is  $E_3$ . The factor  $[1 - \exp((-q_0 - \mu_2 + \mu_4)/T)]^{-1}$  maintains detailed balance, for particles labeled '2' and '4' which are in thermal equilibrium at temperature  $T$  and in chemical equilibrium with chemical potentials  $\mu_2$  and  $\mu_4$ , respectively. The final state blocking of the outgoing lepton is accounted for by the Pauli blocking factor  $(1 - f_3(E_3))$ . The lepton tensor  $L_{\alpha\beta}$  is given by

$$L^{\alpha\beta} = 8[2k^\alpha k^\beta + (k \cdot q)g^{\alpha\beta} - (k^\alpha q^\beta + q^\alpha k^\beta) \mp i\epsilon^{\alpha\beta\mu\nu} k^\mu q^\nu] \quad (43)$$

The target particle retarded polarization tensor is

$$\text{Im}\Pi_{\alpha\beta}^R = \tanh\left(\frac{q_0 + (\mu_2 - \mu_4)}{2T}\right) \text{Im} \Pi_{\alpha\beta}, \quad (44)$$

where  $\Pi_{\alpha\beta}$  is the time ordered or causal polarization and is given by

$$\Pi_{\alpha\beta} = -i \int \frac{d^4p}{(2\pi)^4} \text{Tr} [T(G_2(p)J_\alpha G_4(p+q)J_\beta)]. \quad (45)$$

Above,  $k_\mu$  is the incoming neutrino four-momentum and  $q_\mu$  is the four-momentum transfer. In writing the lepton tensor, we have neglected the electron mass term, since typical electron energies are of the order of a few hundred MeV. The Greens' functions  $G_i(p)$  (the index  $i$  labels particle species) describe the propagation of baryons at finite density and temperature. The current operator  $J_\mu$  is  $\gamma_\mu$  for the vector current and  $\gamma_\mu\gamma_5$  for the axial current. Effects of strong and electromagnetic correlations may be calculated by utilizing the RPA polarization tensor

$$\Pi^{RPA} = \Pi + \Pi^{RPA} D \Pi , \quad (46)$$

where  $D$  denotes the interaction matrix, in Eq. (42) (see [47] for more details).

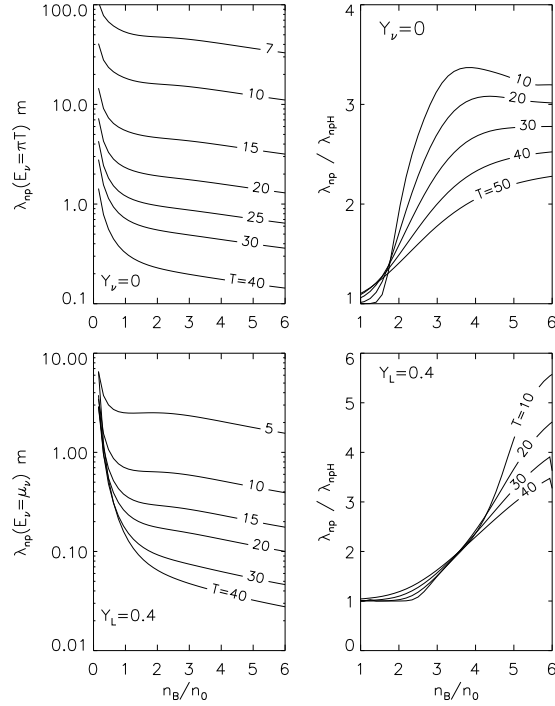


**Fig. 5.** Neutrino mean free paths in matter with nucleons only (left panels). Right panels show ratios of mean free paths in matter without and with hyperons. Abscissa is baryon density  $n_B$  ( $n_0$  is the nuclear equilibrium density). Top panels show scattering mean free paths common to all neutrino species. The bottom panels show results for electron neutrino mean free paths where absorption reactions are included. The neutrino content is labelled in the different panels

#### 4.1 Neutrino Mean Free Paths

The differential cross section (Eq. (42)) is needed in multi-energy group neutrino transport codes. However, more approximate neutrino transport algorithms (as in Section 2) require the total cross section as a function of the neutrino energy for the calculation of diffusion coefficients. The cross section per unit volume of matter (or equivalently the inverse mean free path) is obtained by integrating  $E_3$  and  $\Omega_3$  in Eq. (42).

Under degenerate conditions even modest changes to the composition significantly alter the neutrino scattering and absorption mean free paths. In Fig. 5, the neutrino scattering and absorption mean free paths are shown for models GM3np and GM3npH relevant to the deleptonization and cooling epochs. The top panels show the scattering mean free paths common to all neutrino species in neutrino free matter. The scattering mean free paths for thermal neutrinos ( $E_\nu = \pi T$ ) is shown in the left panel for various temperatures. To study the influence of hyperons, the ratio of the  $\lambda_{np}/\lambda_{npH}$  is shown in the right panels. The presence of hyperons significantly increase the scattering cross sections, by a factor  $\sim (2 - 3)$ . Similar results for the absorption cross sections are shown in the lower panels for  $Y_L = 0.4$ . Again we notice a significant enhancement (right panel) when hyperons appear, the factor here could be as large as 5.

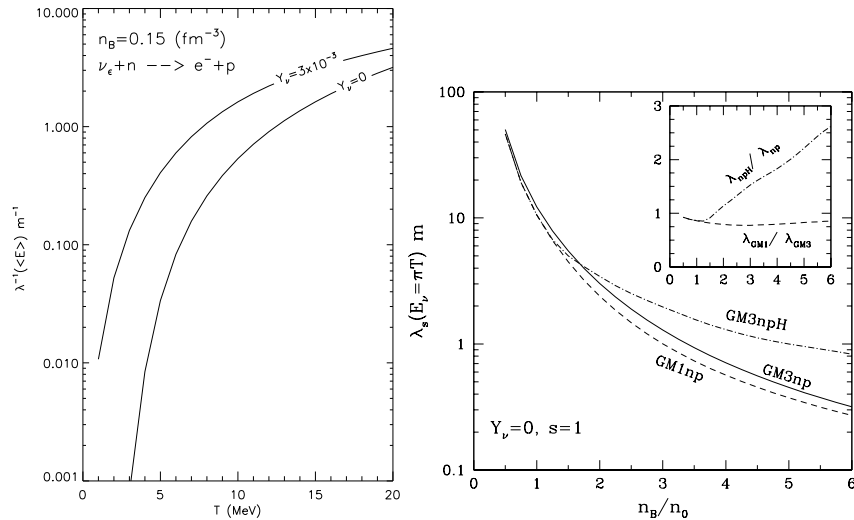


**Fig. 6.** Left: Charged current inverse neutrino mean free paths versus temperature. Right: Comparison of scattering mean free paths in neutrino poor matter at fixed entropy for different EOSs in matter containing nucleons and also hyperons

During the deleptonization stage, lepton number transport is sensitive to charged current reactions which dominate scattering reactions. At zero temperature, charged current reactions  $\nu + n \leftrightarrow e + p$  depend sensitively on the proton

fraction  $Y_p$  [58]. Kinematic restrictions require  $Y_p$  to be larger than 11 – 14% (direct Urca threshold). At early times, a finite neutrino chemical potential favors a large  $Y_p$  throughout the star, which enables these reactions to proceed without any hindrance. Toward the late stages, however,  $Y_p$  decreases with decreasing  $\mu_\nu$  and charged current reactions may be naively expected to become inoperative. The threshold density for the charged current reaction when  $\mu_\nu = 0$  and  $T = 0$  depends sensitively on the density dependence of the nuclear symmetry energy. In field-theoretical models, in which the symmetry energy is largely given by contributions due to  $\rho$ -meson exchange, the critical density is typically  $n_B = 2 \sim 3n_0$ . However, finite temperatures favor larger  $Y_p$ 's and increase the average neutrino energy enabling the charged current reactions to proceed even below these densities. Fig. 6 shows that this is the case even at relatively low temperatures ( $T \sim 3 - 5$ ) MeV for a baryon density  $n_B = 0.15 \text{ fm}^{-3}$ . The sharp rise with temperature, which occurs even for  $Y_\nu = 0$ , clearly indicates that this reaction dominates the  $\nu_e$  opacity even during the late deleptonization era. Thus, charged current reactions cannot be simply turned off when the neutrino chemical potential becomes small enough as was done in prior PNS simulations [1].

The EOS and neutrino mean free paths are intimately related, which is best illustrated by comparing the results shown in Fig. 5 with those shown in Fig. 6. Composition and the baryon effective masses influence both the neutrino mean free paths and the matter's specific heat. Hyperons decrease the neutrino mean free paths at constant temperature Fig. 5. This trend is reversed at constant entropy due to the significantly lower temperatures favored in npH matter. Similar effects are apparent when we compare np models with different baryon effective masses. At a constant temperature, the larger effective mass in model GM3np favors larger cross sections, while at constant entropy this trend is again reversed due to the lower temperatures favored by the larger specific heat.

The diffusion coefficients are calculated using Eq. (18) with the cross sections discussed above. The diffusion coefficients  $D_2$ ,  $D_3$ , and  $D_4$  are functions of  $n_B$ ,  $T$ , and  $Y_{\nu_e}$ .

## 4.2 Inhomogeneous Phases: Effects of First Order Transitions

The thermodynamics of the two situations, first order kaon condensation [15,34] and the quark-hadron transition [37], has been previously considered. Reddy, Bertsch and Prakash [31] have studied the effects of inhomogeneous phases on  $\nu$ -matter interactions. Based on simple estimates of the surface tension between nuclear matter and the exotic phase, typical droplet sizes range from 5 – 15 fm [35], and inter-droplet spacings range up to several times larger. The propagation of neutrinos whose wavelength is greater than the typical droplet size and less than the inter-droplet spacing, i.e.,  $2 \text{ MeV} \lesssim E_\nu \lesssim 40 \text{ MeV}$ , will be greatly affected by the heterogeneity of the mixed phase, as a consequence of the coherent scattering of neutrinos from the matter in the droplet.

The Lagrangian that describes the neutral current coupling of neutrinos to the droplet is

$$\mathcal{L}_W = \frac{G_F}{2\sqrt{2}} \bar{\nu} \gamma_\mu (1 - \gamma_5) \nu J_D^\mu, \quad (47)$$

where  $J_D^\mu$  is the neutral current carried by the droplet and  $G_F = 1.166 \times 10^{-5} \text{ GeV}^{-2}$  is the Fermi weak coupling constant. For non-relativistic droplets,  $J_D^\mu = \rho_W(x) \delta^{\mu 0}$  has only a time like component. Here,  $\rho_W(x)$  is the excess weak charge density in the droplet. The total weak charge enclosed in a droplet of radius  $r_d$  is  $N_W = \int_0^{r_d} d^3x \rho_W(x)$  and the form factor is  $F(q) = (1/N_W) \int_0^{r_d} d^3x \rho_W(x) \sin qx/qx$ . The differential cross section for neutrinos scattering from an isolated droplet is then

$$\frac{d\sigma}{d\cos\theta} = \frac{E_\nu^2}{16\pi} G_F^2 N_W^2 (1 + \cos\theta) F^2(q). \quad (48)$$

In the above equation,  $E_\nu$  is the neutrino energy and  $\theta$  is the scattering angle. Since the droplets are massive, we consider only elastic scattering for which the magnitude of the momentum transfer is  $q = \sqrt{2}E_\nu(1 - \cos\theta)$ .

We must embed the droplets into the medium to evaluate the neutrino transport parameters. The droplet radius  $r_d$  and the inter-droplet spacing are determined by the interplay of surface and Coulomb energies. In the Wigner-Seitz approximation, the cell radius is  $R_W = (3/4\pi N_D)^{1/3}$  where the droplet density is  $N_D$ . Except for one aspect, we will neglect coherent scattering from more than one droplet. If the droplets form a lattice, Bragg scattering will dominate and our description would not be valid. But for low density and a liquid phase, interference from multiple droplets affects scattering only at long wavelengths. If the ambient temperature is not small compared to the melting temperature, the droplet phase will be a liquid and interference effects arising from scattering off different droplets are small for neutrino energies  $E_\nu \gtrsim (1/R_W)$ . However, multiple droplet scattering cannot be neglected for  $E_\nu \lesssim 1/R_W$ . The effects of other droplets is to cancel scattering in the forward direction, because the interference is destructive except at exactly zero degrees, where it produces a change in the index of refraction of the medium. These effects are usually incorporated by multiplying the differential cross section Eq. (48) by the static form factor of the medium. The static form factor, defined in terms of the radial distribution function of the droplets,  $g(r)$ , is

$$S(q) = 1 + N_D \int d^3r \exp i\mathbf{q}\cdot\mathbf{r} (g(r) - 1). \quad (49)$$

The droplet correlations, which determine  $g(r)$ , arise due to the Coulomb force and is measured in terms of the dimensionless Coulomb number  $\Gamma = Z^2 e^2 / (8\pi R_W kT)$ . Due to the long-range character of the Coulomb force, the role of screening and the finite droplet size,  $g(r)$  cannot be computed analytically. We use a simple ansatz for the radial distribution function  $g(r < R_W) = 0$  and  $g(r > R_W) = 1$ . For this choice, the structure factor is independent of  $\Gamma$ . Monte Carlo calculations [59] of the liquid structure function of a simple one

component plasma indicate that our choice of  $S(q)$  is conservative for typical neutrino energies of interest.

The simple ansatz for  $g(r)$  is equivalent to subtracting, from the weak charge density  $\rho_W$ , a uniform density which has the same total weak charge  $N_W$  as the matter in the Wigner-Seitz cell. Thus, effects due to  $S(q)$  may be incorporated by replacing the form factor  $F(q)$  by

$$F(q) \rightarrow \tilde{F}(q) = F(q) - 3 \frac{\sin qR_W - (qR_W) \cos qR_W}{(qR_W)^3}. \quad (50)$$

The neutrino–droplet differential cross section per unit volume then follows:

$$\frac{1}{V} \frac{d\sigma}{d\cos\theta} = N_D \frac{E_\nu^2}{16\pi} G_F^2 N_W^2 (1 + \cos\theta) \tilde{F}^2(q). \quad (51)$$

Note that even for small droplet density  $N_D$ , the factor  $N_W^2$  acts to enhance the droplet scattering. To quantify the importance of droplets as a source of opacity, we compare with the standard scenario in which matter is uniform and composed of neutrons. The dominant source of opacity is then due to scattering from thermal fluctuations and

$$\begin{aligned} \frac{1}{V} \frac{d\sigma}{d\cos\theta} &= \frac{G_F^2}{8\pi} (c_V^2(1 + \cos\theta) + (3 - \cos\theta)c_A^2) E_\nu^2 \\ &\times \frac{3}{2} n_n \left[ \frac{k_B T}{E_{fn}} \right], \end{aligned} \quad (52)$$

where  $c_V$  and  $c_A$  are respectively the vector and axial coupling constants of the neutron,  $n_n$  is the neutron number density,  $E_{fn}$  is the neutron Fermi energy and  $T$  is the matter temperature [60].

The transport cross sections that are employed in studying the diffusive transport of neutrinos in the core of a neutron star are differential cross sections weighted by the angular factor  $(1 - \cos\theta)$ . The transport mean free path  $\lambda(E_\nu)$  for a given neutrino energy  $E_\nu$  is given by

$$\frac{1}{\lambda(E_\nu)} = \frac{\sigma_T(E_\nu)}{V} = \int d\cos\theta (1 - \cos\theta) \left[ \frac{1}{V} \frac{d\sigma}{d\cos\theta} \right]. \quad (53)$$

Models of first order phase transitions in dense matter provide the weak charge and form factors of the droplets and permit the evaluation of  $\nu$ –droplet scattering contributions to the opacity of the mixed phase. For the models considered, namely the first order kaon condensate and the quark-hadron phase transition, the neutrino mean free paths in the mixed phase are shown in the left and right panels of Fig. 7, respectively. The results are shown for the indicated values of the baryon density  $n_B$  and temperature  $T$  where the model predicts a mixed phase exists. The kaon droplets are characterized by radii  $r_d \sim 7$  fm and inter-droplet spacings  $R_W \sim 20$  fm, and enclose a net weak vector charge  $N_W \sim 700$ . The quark droplets are characterized by  $r_d \sim 5$  fm and  $R_W \sim 11$  fm, and an enclosed weak charge  $N_W \sim 850$ . For comparison, the neutrino mean

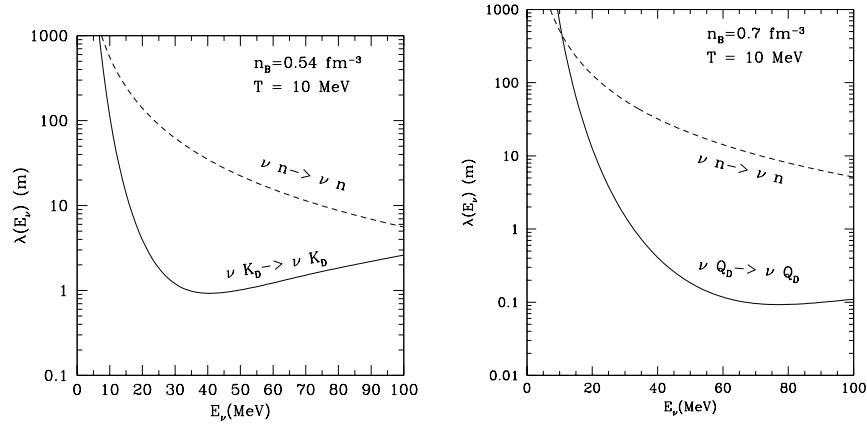


**Fig. 7.** Neutrino mean free paths as a function of neutrino energy. Solid lines are for matter in a mixed phase containing kaons (left panel) and quarks (right panel), and dashed curves are for uniform matter.

free path in uniform neutron matter at the same  $n_b$  and  $T$  are also shown. It is apparent that there is a large coherent scattering-induced reduction in the mean free path for the typical energy  $E_\nu \sim \pi T$ . At much lower energies, the inter-droplet correlations tend to screen the weak charge of the droplet, and at higher energies the coherence is attenuated by the droplet form factor.

The large reduction in neutrino mean free path found here implies that the mixed phase will cool significantly slower than homogeneous matter. Consequently, the observable neutrino luminosity at late times might be affected as it is driven by the transport of energy from the deep interior. The reduced mean free path in the interior will tend to prolong the late time neutrino emission phase.

### 4.3 Effects of Quark Superconductivity and Superfluidity

Recent theoretical works [61,62] suggest that quarks form Cooper pairs in medium, a natural consequence of attractive interactions destabilizing the Fermi surface. Although the idea of quark pairing in dense matter is not new [61,63], it has recently seen renewed interest in the context of the phase diagram of QCD [62]. Model calculations, mostly based on four-quark effective interactions, predict the restoration of spontaneously broken chiral symmetry through the onset of color superconductivity at low temperatures. They predict an energy gap of  $\Delta \sim 100$  MeV for a typical quark chemical potential of  $\mu_q \sim 400$  MeV. As in BCS theory, the gap will weaken for  $T > 0$ , and at some critical temperature  $T_c$  there is a (second-order) transition to a “standard” quark-gluon plasma. During cooling from an initial temperature in excess of  $T_c$ , the formation of a gap in the fermionic excitation spectrum in quark matter will influence various transport



properties of the system. Carter and Reddy have studied its influence on the transport of neutrinos [64].

The differential neutrino scattering cross section per unit volume in an infinite and homogeneous system of relativistic fermions as calculated in linear response theory is given by Eq. (42). The medium is characterized by the quark polarization tensor  $\Pi_{\alpha\beta}$ . In the case of free quarks, each flavor contributes a term of the form

$$\Pi_{\alpha\beta}(q) = -i\text{Tr}_c \int \frac{d^4p}{(2\pi)^4} \text{Tr} [S_0(p)\Gamma_\alpha S_0(p+q)\Gamma_\beta], \quad (54)$$

where  $S_0(p)$  is the free quark propagator at finite chemical potential and temperature. The outer trace is over color and simplifies to a  $N_c = 3$  degeneracy. The inner trace is over spin, and the  $\Gamma_\alpha$  are the neutrino-quark vertex functions which determine the spin channel. Specifically, the vector polarization is computed by choosing  $(\Gamma_\alpha, \Gamma_\beta) = (\gamma_\alpha, \gamma_\beta)$ . The axial and mixed vector-axial polarizations are similarly obtained from  $(\Gamma_\alpha, \Gamma_\beta) = (\gamma_\alpha\gamma_5, \gamma_\beta\gamma_5)$  and  $(\Gamma_\alpha, \Gamma_\beta) = (\gamma_\alpha, \gamma_\beta\gamma_5)$ , respectively.

The free quark propagators in Eq. (54) are naturally modified in a superconducting medium. As first pointed out by Bardeen, Cooper, and Schrieffer several decades ago, the quasi-particle dispersion relation is modified due to the presence of a gap in the excitation spectrum. In calculating these effects, we will consider the simplified case of QCD with two quark flavors which obey  $SU(2)_L \times SU(2)_R$  flavor symmetry, given that the light  $u$  and  $d$  quarks dominate low-energy phenomena. Furthermore we will assume that, through some unspecified effective interactions, quarks pair in a manner analogous to the BCS mechanism [65]. The relevant consequences of this are the restoration of chiral symmetry (hence all quarks are approximately massless) and the existence of an energy gap at zero temperature,  $\Delta_0$ , with approximate temperature dependence,

$$\Delta(T) = \Delta_0 \sqrt{1 - \left(\frac{T}{T_c}\right)^2}. \quad (55)$$

The critical temperature  $T_c \simeq 0.57\Delta_0$  is likewise taken from BCS theory; this relation has been shown to hold for perturbative QCD [66] and is thus a reasonable assumption for non-perturbative physics.

Breaking the  $SU_c(3)$  color group leads to complications not found in electrodynamics. In QCD the superconducting gap is equivalent to a diquark condensate, which can at most involve two of the three fundamental quark colors. The condensate must therefore be colored. Since the scalar diquark (in the  $\bar{\mathbf{3}}$  color representation) appears to always be the most attractive channel, we consider the anomalous (or Gorkov) propagator [67]

$$\begin{aligned} F(p)_{abfg} &= \langle q_{fa}^T(p) C \gamma_5 q_{gb}(-p) \rangle \\ &= -i\epsilon_{ab3}\epsilon_{fg} \Delta \left( \frac{\Lambda^+(p)}{p_o^2 - \xi_p^2} + \frac{\Lambda^-(p)}{p_o^2 - \bar{\xi}_p^2} \right) \gamma_5 C. \end{aligned} \quad (56)$$

Here,  $a, b$  are color indices,  $f, g$  are flavor indices,  $\epsilon_{abc}$  is the usual anti-symmetric tensor and we have conventionally chosen 3 to be the condensate color. This propagator is also antisymmetric in flavor and spin, with  $C = -i\gamma_0\gamma_2$  being the charge conjugation operator.

The color bias of the condensate forces a splitting of the normal quark propagator into colors transverse and parallel to the diquark. Quarks of color 3, parallel to the condensate in color space, will be unaffected and propagate freely, with

$$S_0(p)_{af}^{bg} = i\delta_a^b\delta_f^g \left( \frac{\Lambda^+(p)}{p_o^2 - E_p^2} + \frac{\Lambda^-(p)}{p_o^2 - \bar{E}_p^2} \right) (p_\mu\gamma^\mu - \mu\gamma_0). \quad (57)$$

This is written in terms of the particle and anti-particle projection operators  $\Lambda^+(p)$  and  $\Lambda^-(p)$  respectively, where  $\Lambda^\pm(p) = (1 \pm \gamma_0\boldsymbol{\gamma} \cdot \hat{p})/2$ . The excitation energies are simply  $E_p = |\mathbf{p}| - \mu$  for quarks and  $\bar{E}_p = |\mathbf{p}| + \mu$  for anti-quarks.

On the other hand, transverse quark colors 1 and 2 participate in the diquark and thus their quasi-particle propagators are given as

$$S(p)_{af}^{bg} = i\delta_a^b\delta_f^g \left( \frac{\Lambda^+(p)}{p_o^2 - \xi_p^2} + \frac{\Lambda^-(p)}{p_o^2 - \bar{\xi}_p^2} \right) (p_\mu\gamma^\mu - \mu\gamma_0). \quad (58)$$

The quasi-particle energy is  $\xi_p = \sqrt{(|\mathbf{p}| - \mu)^2 + \Delta^2}$ , and for the anti-particle  $\bar{\xi}_p = \sqrt{(|\mathbf{p}| + \mu)^2 + \Delta^2}$ .

The appearance of an anomalous propagator in the superconducting phase indicates that the polarization tensor gets contributions from both the normal quasi-particle propagators Eq. (58) and anomalous propagator Eq. (56). Thus, to order  $G_F^2$ , Eq. (54) is replaced with the two contributions corresponding to the diagrams shown in Fig. 8, and written

$$\begin{aligned} \Pi_{\alpha\beta}(q) &= -i \int \frac{d^4p}{(2\pi)^4} \{ \text{Tr} [S_0(p)\Gamma_\alpha S_0(p+q)\Gamma_\beta] \\ &\quad + 2\text{Tr} [S(p)\Gamma_\alpha S(p+q)\Gamma_\beta] + 2\text{Tr} [F(p)\Gamma_\alpha \bar{F}(p+q)\Gamma_\beta] \}. \end{aligned} \quad (59)$$

The remaining trace is over spin, as the color trace has been performed. Fig. 8(a) corresponds to the first two terms, which have been decomposed into one term with ungapped propagators Eq. (57) and the other with gapped quasi-particle propagators Eq. (58). Fig. 8(b) represents the third, anomalous term.

For neutrino scattering we must consider vector, axial, and mixed vector-axial channels, all summed over flavors. The full polarization, to be used in evaluating Eq. (42), may be written

$$\Pi_{\alpha\beta} = \sum_f \left[ (C_V^f)^2 \Pi_{\alpha\beta}^V + (C_A^f)^2 \Pi_{\alpha\beta}^A - 2C_V^f C_A^f \Pi_{\alpha\beta}^{VA} \right]. \quad (60)$$

The coupling constants for up quarks are  $C_V^u = \frac{1}{2} - \frac{4}{3}\sin^2\theta_W$  and  $C_A^u = \frac{1}{2}$ , and for down quarks,  $C_V^d = -\frac{1}{2} + \frac{2}{3}\sin^2\theta_W$  and  $C_A^d = -\frac{1}{2}$ , where  $\sin^2\theta_W \simeq 0.23$  is the Weinberg angle.

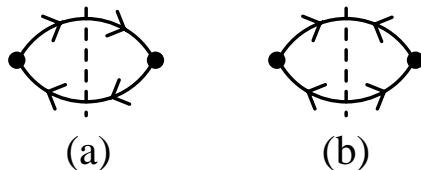


**Fig. 8.** Standard loop (a) and anomalous loop (b) diagrams contributing to the quark polarization operator

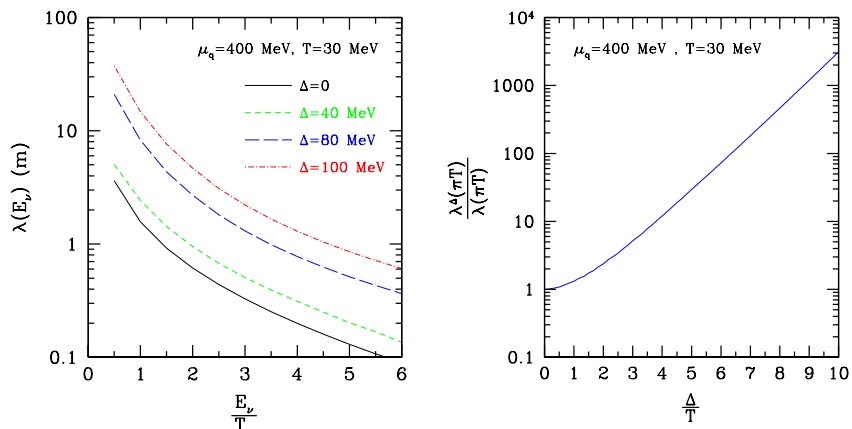


**Fig. 9.** Left panel: Neutrino mean free path as a function of neutrino energy  $E_\nu$ . Right panel: Neutrino mean free paths for  $E_\nu = \pi T$  as a function of  $\Delta/T$ . These results are virtually independent of temperature for  $T \lesssim 50$  MeV.

The differential cross section, Eq. (42) and the total cross section are obtained by integrating over all neutrino energy transfers and angles. Results for the neutrino mean free path,  $\lambda = V/\sigma$ , are shown in Fig. 9 as a function of incoming neutrino energy  $E_\nu$  (for ambient conditions of  $\mu_q = 400$  MeV and  $T = 30$  MeV). They show the same energy dependence found previously for free relativistic and degenerate fermionic matter [46];  $\lambda \propto 1/E_\nu^2$  for  $E_\nu \gg T$  and  $\lambda \propto 1/E_\nu$  for  $E_\nu \ll T$ . The results indicate that this energy dependence is not modified by the presence of a gap when  $\Delta \sim T$ . Thus, the primary effect of the superconducting phase is a much larger mean free path. This is consistent with the suppression found in the vector-longitudinal response function, which dominates the polarization sum Eq. (60), at  $q_0 < q$ .

We now consider the cooling of a macroscopic sphere of quark matter, a toy approximation for the core of a neutron star with a mixed quark phase, as it becomes superconducting. As in the preceding calculation, we consider the relatively simple case of two massless flavors with identical chemical potentials and disregard the quarks parallel in color to the condensate; *i.e.* we consider a background comprised exclusively of quasi-quarks.

The cooling of a spherical system of quark matter from  $T \sim T_c \sim 50$  MeV is driven by neutrino diffusion, for the neutrino mean free path is much smaller than the dimensions of system of astrophysical size, and yet several orders of magnitude larger than the mean free path of the quarks. The diffusion equation for energy transport by neutrinos in a spherical geometry is

$$C_V \frac{dT}{dt} = -\frac{1}{r^2} \frac{\partial L_\nu}{\partial r}, \quad (61)$$

where  $C_V$  is the specific heat per unit volume of quark matter,  $T$  is the temperature, and  $r$  is the radius. The neutrino energy luminosity for each neutrino type,  $L_\nu$ , depends on the neutrino mean free path and the spatial gradients in temperature and is approximated by an integral over neutrino energy  $E_\nu$

$$L_\nu \cong 6 \int dE_\nu \frac{c}{6\pi^2} E_\nu^3 r^2 \lambda(E_\nu) \left| \frac{\partial f(E_\nu)}{\partial r} \right|. \quad (62)$$

We assume that neutrino interactions are dominated by the neutral current scattering which is common to all neutrino types, accounting for the factor 6 in Eq. (62).

The solution to the diffusion equation will depend on the initial temperature gradients. However, being primarily interested in a qualitative description of cooling through a second-order phase transition to superconducting matter, the temporal behavior can be characterized by a time scale  $\tau_c$  which is proportional to the inverse cooling rate. This characteristic time is

$$\tau_c(T) = C_V(T) \frac{R^2}{c \langle \lambda(T) \rangle}, \quad (63)$$

and is a strong function of the temperature since it depends on both the specific heat  $C_V$  and the energy-averaged neutrino mean free path,  $\langle \lambda(T) \rangle$ . The latter quantity is here approximated by  $\lambda(E_\nu = \pi T)$  since the neutrinos are in thermal equilibrium. Using BCS theory, as described in the previous section,  $\langle \lambda(T) \rangle$  depends on the gap  $\Delta$  as shown in the right panel of Fig. 9. The results indicate that for small  $\Delta/T$ ,  $\lambda$  is not strongly modified, but as  $\Delta/T$  increases so too does  $\lambda$ , non-linearly at first and then exponentially for  $\Delta/T \gtrsim 5$ . Also, in the BCS theory, the temperature dependences of  $C_V$  (dashed curve) and  $\Delta$  (dot-dashed curve) are shown in Fig. 10. Finally, the ratio  $\tau_c^\Delta(T)/\tau_c(T)$ , a measure of the extent to which the cooling rate is changed by a gap, is shown by the solid line in Fig. 10. We note that the diffusion approximation is only valid when  $\lambda \ll R$  and will thus fail for very low temperatures, when  $\lambda \lesssim R$ .

These results are readily interpreted. The cooling rate around  $T_c$  is influenced mainly by the peak in the specific heat associated with the second order phase transition, since the neutrino mean free path is not strongly affected when  $T \geq \Delta$ . Subsequently, as the matter cools, both  $C_V$  and  $\lambda^{-1}$  decrease in a non-linear fashion for  $T \sim \Delta$ . Upon further cooling, when  $T \ll \Delta$ , both  $C_V$  and  $\lambda^{-1}$  decrease exponentially. Both effects accelerate the cooling process.

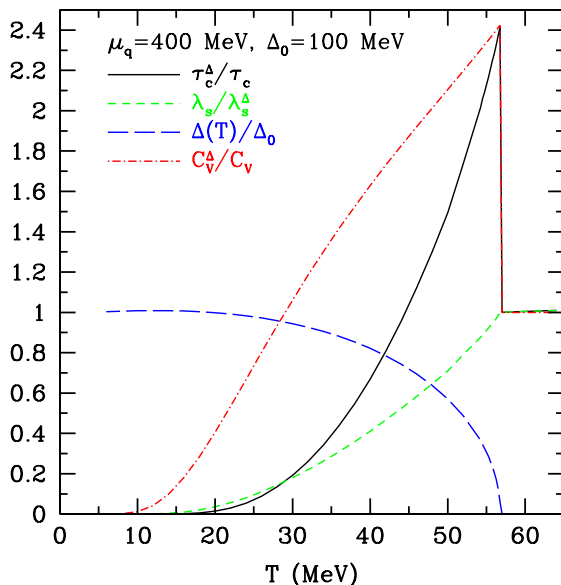


**Fig. 10.** The extent to which different physical quantities are affected by a superconducting transition. Ratios of the cooling time scale (solid curve), the inverse mean free path (short-dashed curve) and the matter specific heat (dot-dashed curve) in the superconducting phase to that in the normal phase is shown as a function of the matter temperature. The ratio of the gap to its zero temperature value  $\Delta_0$  is also shown (long-dashed curve).

We conclude that if it were possible to measure the neutrino luminosity from the hypothetical object described here, a second order superconducting transition might be identified by the temporal characteristics of the late time supernova neutrino signal from a PNS. Specifically, there might be a brief interval during which the cooling would slow when the core temperature falls below  $T_c$ , signified by a period of reduced neutrino detection. However, this effect might be obscured by  $\nu$ -opaque matter outside the star's core. If the neutrino opacity of these outer regions of the star is large, it is likely that any sharp temporal feature associated with neutrino transport in the core will be diluted as the neutrino diffuse through the outer regions. Nevertheless, the main finding, which is that phase transitions in the core can have a discernible impact on the transport of neutrinos and suggests that the late time supernova neutrino signal is a promising probe of the high density and low temperature region of the QCD phase diagram.

## 5 Results of PNS Simulations

Neutrino signals from PNSs depends on many stellar properties, including the mass; initial entropy, lepton fraction and density profiles; and neutrino opaci-

ties. Pons et al. [10] carried out a detailed study of the dependence of neutrino emission on PNS characteristics. They verified the generic results of Burrows & Lattimer [1] that both neutrino luminosities and average energies increased with increasing mass (see Fig. 11). In addition, they found that variations in initial entropy and lepton fraction profiles in the outer regions of the PNS caused only transient (lasting a few tenths of a second) variations in neutrino luminosities and energies. Variations in the central lepton fraction and entropy were found to produce modest changes in neutrino luminosities that persisted to late times. The central values of lepton fraction and entropy are established during core collapse, and will depend upon the initial properties of the star as well as the EOS and neutrino transport during the collapse.

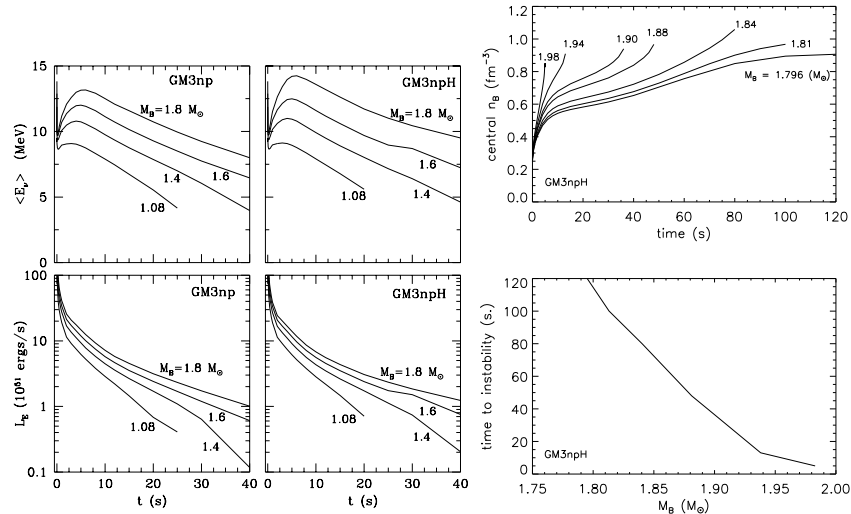


**Fig. 11.** Left: The evolution of the neutrino average energy and total neutrino luminosity is compared for several assumed PNS baryon masses and EOSs. The EOSs in the left panels contain only baryons and leptons while those in the right panels also contain hyperons. Top right panel: Evolution of the central baryon number density for different baryonic mass stars containing hyperons (model GM3npH) which are metastable. Bottom right panel: Time required by stars shown in the top panel to reach the unstable configuration

## 5.1 Baseline Results

Properties of the dense matter EOS that affect PNS evolution include the compressibility, symmetry energy, specific heat, and composition. Pons et al. [10] employed a field theoretical EOS [4], with which the results due to some differences in stellar size (due to variations in nuclear interactions) and composition were studied. Some results are summarized in Fig. 11. Overall, both the average

energies and luminosities of stars containing hyperons were larger compared to those without. In addition, for stars without hyperons, those stars with smaller radii had higher average emitted neutrino energy, although the predicted luminosities for early times ( $t < 10$  s) were insensitive to radii. This result only holds if the opacities are calculated consistently with each EOS [46,47]; otherwise rather larger variations in evolutions would have been found [42,48]. The same held true for models which allowed for the presence of hyperons, except when the initial proto-neutron star mass was significantly larger than the maximum mass for cold, catalyzed matter. Another new result was that the average emitted neutrino energy of all flavors increased during the first 2-5 seconds of evolution, and then decreased nearly linearly with time. For times larger than about 10 seconds, and prior to the occurrence of neutrino transparency, the neutrino luminosities decayed exponentially with a time constant that was sensitive to the high-density properties of matter. Significant variations in neutrino emission occurred beyond 10 seconds: it was found that neutrino luminosities were larger during this time for stars with smaller radii and with the inclusion of hyperons in the matter. Finally, significant regions of the stars appeared to become convectively unstable during the evolution, as several works have found [68,69,70,71,72].

The right panel of Fig. 11 shows the time development of the central baryon density (top panel) and also the time to the collapse instability as a function of baryon mass (bottom panel). The larger the mass, the shorter the time to instability, since the PNS does not have to evolve in lepton number as much. Above  $2.005 M_{\odot}$ , the metastability disappears because the GM3npH initial model with the lepton and entropy profiles we chose is already unstable. Below about  $1.73 M_{\odot}$ , there is no metastability, since this is the maximum mass of the cold, catalyzed npH star for GM3. The signature of neutrino emission from a metastable PNS should be identifiable and it is discussed in Section 5.4.

## 5.2 Influence of Many-Body Correlations

The main effect of the larger mean free paths produced by RPA corrections [47] is that the inner core deleptonizes more quickly. In turn, the maxima in central temperature and entropy are reached on shorter timescales. In addition, the faster increase in thermal pressure in the core slows the compression associated with the deleptonization stage, although after 10 s the net compressions of all models converge.

The relatively large, early, changes in the central thermodynamic variables do not, however, translate into similarly large effects on observables such as the total neutrino luminosity and the average radiated neutrino energy, relative to the baseline simulation. The luminosities for the different models are shown as a function of time in Fig. 12. The left panel shows the early time development in detail. The exploratory models agree with the results reported in [48,49]. However, the magnitude of the effects when full RPA corrections are applied is somewhat reduced compared to the exploratory models. It is especially important that at and below nuclear density, the corrections due to correlations are

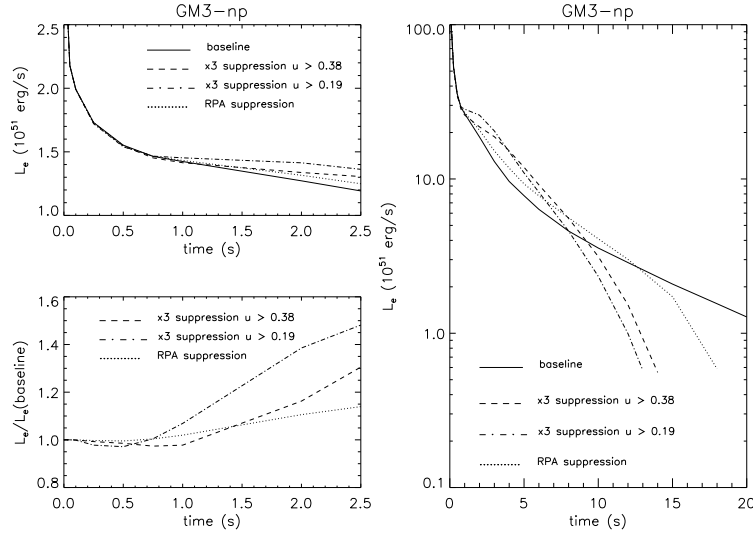


**Fig. 12.** Left: The upper panel shows the total emitted neutrino luminosity for the PNS evolutions described in Reddy et al. [47]. The lower panel shows the ratio of the luminosities obtained in the three models which contain corrections to the baseline (Hartree approximation) model. Right: Emitted neutrino luminosity for long-term PNS evolutions

relatively small. Since information from the inner core is transmitted only by the neutrinos, the time scale to propagate any high density effect to the neutrinosphere is the neutrino diffusion time scale. Since the neutrinosphere is at a density approximately 1/100 of nuclear density, and large correlation corrections occur only above 1/3 nuclear density where nuclei disappear, we find that correlation corrections calculated here have an effect at the neutrinosphere only after 1.5 s. Moreover, the RPA suppression we have calculated is considerably smaller than those reported in [48,49], reaching a maximum of about 30% after 5 s, compared to a luminosity increase of 50% after only 2 s. However, the corrections are still very important during the longer-term cooling stage (see Fig. 12), and result in a more rapid onset of neutrino transparency compared to the Hartree results.

### 5.3 Signals in Detectors

In Fig. 13 the lifetimes versus  $M_B$  for stars containing hyperons ( $npH$ ) and  $npK$  stars are compared [73]. In both cases, the larger the mass, the shorter the lifetime. For kaon-rich PNSs, however, the collapse is delayed until the final stage of the Kelvin-Helmholtz epoch, while this is not necessarily the case for hyperon-rich stars.

In Fig. 14 the evolution of the total neutrino energy luminosity is shown for different models. Notice that the drop in the luminosity for the stable star



(solid line), associated with the end of the Kelvin-Helmholtz epoch, occurs at approximately the same time as for the metastable stars with somewhat higher masses. In all cases, the total luminosity at the end of the simulations is below  $10^{51}$  erg/s. The two upper shaded bands correspond to SN 1987A detection limits with KII and IMB, and the lower bands correspond to detection limits in SNO and SuperK for a future galactic supernova at a distance of 8.5 kpc. The times when these limits intersect the model luminosities indicate the approximate times at which the count rate drops below the background rate  $(dN/dt)_{BG} = 0.2$  Hz.

The poor statistics in the case of SN 1987A precluded a precise estimate of the PNS mass. Nevertheless, had a collapse to a black hole occurred in this case, it must have happened after the detection of neutrinos ended. Thus the SN 1987A signal is compatible with a late kaonization-induced collapse, as well as a collapse due to hyperonization or to the formation of a quark core. More information would be extracted from the detection of a galactic SN with the new generation of neutrino detectors.

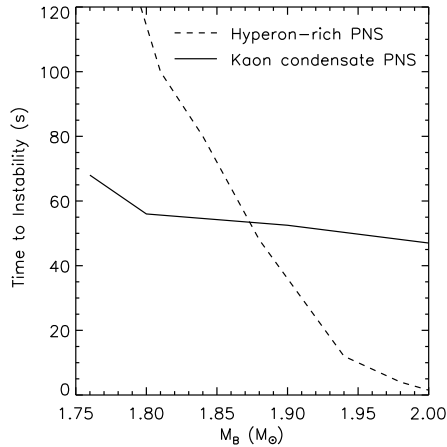


**Fig. 13.** Lifetimes of metastable stars as a function of the stellar baryon mass. Solid lines show results for PNSs containing kaon-condensates and dashed lines show the results of Pons, et al. [10] for PNSs containing hyperons

In SNO, about 400 counts are expected for electron antineutrinos from a supernova located at 8.5 kpc. The statistics would therefore be improved significantly compared to the observations of SN 1987A. A sufficiently massive PNS with a kaon condensate becomes metastable, and the neutrino signal terminates, before the signal decreases below the assumed background. In SuperK, however, up to 6000 events are expected for the same conditions (because of the larger fiducial mass) and the effects of metastability due to condensate formation in lower mass stars would be observable.

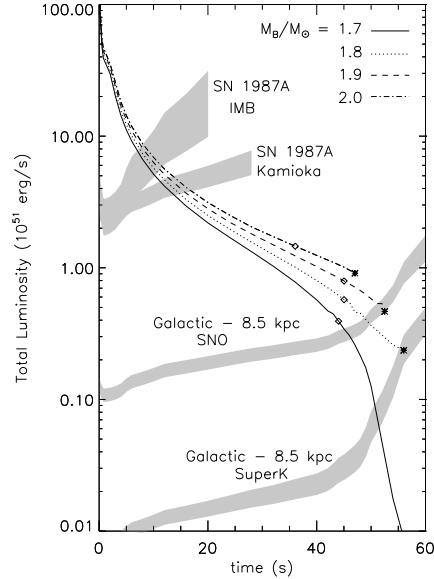


**Fig. 14.** The evolution of the total neutrino luminosity for stars of various baryon masses. Shaded bands illustrate the limiting luminosities corresponding to a count rate of 0.2 Hz in all detectors, assuming a supernova distance of 50 kpc for IMB and Kamioka, and 8.5 kpc for SNO and SuperK. The width of the shaded regions represents uncertainties in the average neutrino energy from the use of a diffusion scheme for neutrino transport

#### 5.4 What Can We Learn From Neutrino Detections?

The calculations of Pons, et al. [73] show that the variations in the neutrino light curves caused by the appearance of a kaon condensate in a stable star are small, and are apparently insensitive to large variations in the opacities assumed for them. Relative to a star containing only nucleons, the expected signal differs by an amount that is easily masked by an assumed PNS mass difference of  $0.01 - 0.02 M_\odot$ . This is in spite of the fact that, in some cases, a first order phase transition appears at the star's center. The manifestations of this phase transition are minimized because of the long neutrino diffusion times in the star's core and the Gibbs' character of the transition. Both act in tandem to prevent either a "core-quake" or a secondary neutrino burst from occurring during the Kelvin-Helmholtz epoch.

Observable signals of kaon condensation occur only in the case of metastable stars that collapse to a black hole. In this case, the neutrino signal for a star closer than about 10 kpc is expected to suddenly stop at a level well above that of the background in a sufficiently massive detector with a low energy threshold such as SuperK. This is in contrast to the signal for a normal star of similar mass for which the signal continues to fall until it is obscured by the background. The lifetime of kaon-condensed metastable stars has a relatively small range, of order

50–70 s for the models studied here, which is in sharp contrast to the case of hyperon-rich metastable stars for which a significantly larger variation in the lifetime (a few to over 100 s) was found. This feature of kaon condensation suggests that stars that destabilize rapidly cannot do so because of kaons.

Pons, et al. [73] determined the minimum lifetime for metastable stars with kaons to be about 40 s by examining the most favorable case for kaon condensation, which is obtained by maximizing the magnitude of the optical potential. The maximum optical potential is limited by the binary pulsar mass constraint, which limits the star’s maximum gravitational mass to a minimum value of  $1.44 M_{\odot}$ . Therefore, should the neutrino signal from a future supernova abruptly terminate sooner than 40 s after the birth of the PNS, it would be more consistent with a hyperon- or quark-induced instability than one due to kaon condensation.

It is important to note that the collapse to a black hole in the case of kaon condensation is delayed until the final stages of the Kelvin-Helmholtz epoch, due to the large neutrino diffusion time in the inner core. Consequently, to distinguish between stable and metastable kaon-rich stars through observations of a cessation of a neutrino signal from a galactic supernovae is only possible using sufficiently massive neutrino detectors with low energy thresholds and low backgrounds, such as the current SNO and SuperK, and future planned detectors including the UNO.

### 5.5 Expectations From Quark Matter

Strangeness appearing in the form of a mixed phase of strange quark matter also leads to metastability. Although quark matter is also suppressed by trapped neutrinos [37,22], the transition to quark matter can occur at lower densities than the most optimistic kaon case, and the dependence of the threshold density on  $Y_L$  is less steep than that for kaons. Thus, it is an expectation that metastability due to the appearance of quarks, as for the case of hyperons, might be able to occur relatively quickly. Steiner, et al. [22] have demonstrated that the temperature along adiabats in the quark-hadron mixed phase is much smaller than what is found for the kaon condensate-hadron mixed phase. Calculations of PNS evolution with a mixed phase of quark matter, including the possible effects of quark matter superfluidity [64] are currently in progress and will be reported separately.

## 6 Long-Term Cooling: The Next Million Years

Following the transparency of the neutron star to neutrinos, the only observational link with these objects is through photon emissions, either as a pulsar or through thermal emissions or both. Thermal emissions of course are controlled by the temperature evolution of the star, and this depends sensitively upon its internal composition. The tabulation of temperatures and ages for a set of neutron stars would go a long way to deciding among several possibilities.

### 6.1 Thermal Evolution

The cooling of a young (age  $< 10^5$  yr) neutron star is mainly governed by  $\nu$ -emission processes and the specific heat [74]. Due to the extremely high thermal conductivity of electrons, a neutron star becomes nearly isothermal within a time  $t_w \approx 1 - 100$  years after its birth, depending upon the thickness of the crust [7]. After this time its thermal evolution is controlled by energy balance:

$$\frac{dE_{th}}{dt} = C_V \frac{dT}{dt} = -L_\gamma - L_\nu + H, \quad (64)$$

where  $E_{th}$  is the total thermal energy and  $C_V$  is the specific heat.  $L_\gamma$  and  $L_\nu$  are the total luminosities of photons from the hot surface and  $\nu$ s from the interior, respectively. Possible internal heating sources, due, for example, to the decay of the magnetic field or friction from differential rotation, are included in  $H$ . Our cooling simulations were performed by solving the heat transport and hydrostatic equations including general relativistic effects (see [74]). The surface's effective temperature  $T_e$  is much lower than the internal temperature  $T$  because of a strong temperature gradient in the envelope. Above the envelope lies the atmosphere where the emerging flux is shaped into the observed spectrum from which  $T_e$  can be deduced. As a rule of thumb  $T_e/10^6 \text{ K} \approx \sqrt{T/10^8 \text{ K}}$ , but modifications due to magnetic fields and chemical composition may occur.

### 6.2 Rapid vs. Slow Cooling

The simplest possible  $\nu$  emitting processes are the direct Urca processes  $f_1 + \ell \rightarrow f_2 + \nu_\ell$ ,  $f_2 \rightarrow f_1 + \ell + \bar{\nu}_\ell$ , where  $f_1$  and  $f_2$  are either baryons or quarks and  $\ell$  is either an electron or a muon. These processes can occur whenever momentum conservation is satisfied among  $f_1$ ,  $f_2$  and  $\ell$  (within minutes of birth, the  $\nu$  chemical potential vanishes). If the unsuppressed direct Urca process for *any* component occurs, a neutron star will rapidly cool because of enhanced emission: the star's interior temperature  $T$  will drop below  $10^9$  K in minutes and reach  $10^7$  K in about a hundred years.  $T_e$  will hence drop to less than 300,000 K after the crustal diffusion time  $t_w$  [7,75,76]. This is the so-called rapid cooling paradigm. If no direct Urca processes are allowed, or they are all suppressed, cooling instead proceeds through the significantly less rapid modified Urca process in which an additional fermion enables momentum conservation. This situation could occur if no hyperons are present, or the nuclear symmetry energy has a weak density dependence [58,77]. The  $\nu$  emission rates for the nucleon, hyperon, and quark Urca and modified Urca processes can be found in [78].

### 6.3 Superfluid and Superconducting Gaps

Pairing is unavoidable in a degenerate Fermi liquid if there is an attractive interaction in *any* channel. The resulting superfluidity, and in the case of charged particles, superconductivity, in neutron star interiors has a major effect on the

star's thermal evolution through suppressions of neutrino ( $\nu$ ) emission processes and specific heats [74,75]. Neutron ( $n$ ), proton ( $p$ ) and  $\Lambda$ -hyperon superfluidity in the  $^1S_0$  channel and  $n$  superfluidity in the  $^3P_2$  channel have been shown to occur with gaps of a few MeV or less [79,80]. However, the density ranges in which gaps occur remain uncertain. At large baryon densities for which perturbative QCD applies, pairing gaps have been estimated to be a few MeV [63]. However, the pairing gaps of unlike quarks ( $ud$ ,  $us$ , and  $ds$ ) have been suggested to be several tens to hundreds of MeV through non-perturbative studies [62] kindling interest in quark superfluidity and superconductivity [81,82] and their effects on neutron stars [83,84].

The effect of the pairing gaps on the emissivities and specific heats for massive baryons are investigated in [85] and are here generalized to the case of quarks. The principal effects are severe suppressions of both the emissivity and specific heat when  $T \ll \Delta$ , where  $\Delta$  is the pairing gap. In a system in which several superfluid species exist the most relevant gap for these suppressions is the smallest one. The specific heat suppression is never complete, however, because leptons remain unpaired. Below the critical temperature  $T_c$ , pairs may recombine, resulting in the emission of  $\nu\bar{\nu}$  pairs with a rate that exceeds the modified Urca rate below  $10^{10}$  K [86]; these processes are included in our calculations.

The baryon and quark pairing gaps we adopt are shown in Fig. 15. Note that gaps are functions of Fermi momenta ( $p_F(i)$ ,  $i$  denoting the species) which translates into a density dependence. For  $p_F(n, p) \lesssim 200 - 300$  MeV/ $c$ , nucleons pair in the  $^1S_0$  state, but these momenta correspond to densities too low for enhanced  $\nu$  emission involving nucleons to occur. At higher  $p_F$ 's, baryons pair in higher partial waves. The  $n$   $^3P_2$  gap has been calculated for the Argonne V<sub>18</sub>, CD-Bonn and Nijmegen I & II interactions [79]. This gap is crucial since it extends to large  $p_F(n)$  and can reasonably be expected to occur at the centers of neutron stars. For  $p_F(n) > 350$  MeV/ $c$ , gaps are largely uncertain because of both experimental and theoretical uncertainties [79]. The curves [a], [b] and [c] in Fig. 15 reflect the range of uncertainty. The  $p$   $^3P_2$  gap is too small to be of interest. Gaps for the  $^1S_0$  pairing of  $\Lambda$ , taken from [80] and shown as dotted curves, are highly relevant since  $\Lambda$ s participate in direct Urca emission as soon as they appear [77]. Experimental information beyond the  $^1S_0$  channel for  $\Lambda$  is not available.  $\Delta$ s for  $\Sigma$ -hyperons remain largely unexplored. The quark ( $q$ ) gaps are taken to be Gaussians centered at  $p_F(q) = 400$  MeV/ $c$  with widths of 200 MeV/ $c$  and heights of 100 MeV [model D], 10 MeV [C], 1 MeV [B] and 0.1 MeV [A], respectively. The reason for considering quark gaps much smaller than suggested in [62,63] is associated with the multicomponent nature of charge-neutral, beta-equilibrated, neutron star matter as will become clear shortly.

#### 6.4 Effects of Composition

We consider four generic compositions: charge-neutral, beta equilibrated matter containing nucleons only ( $np$ ), nucleons with quark matter ( $npQ$ ), nucleons and hyperons ( $npH$ ), and nucleons, hyperons and quarks ( $npHQ$ ). In the cases

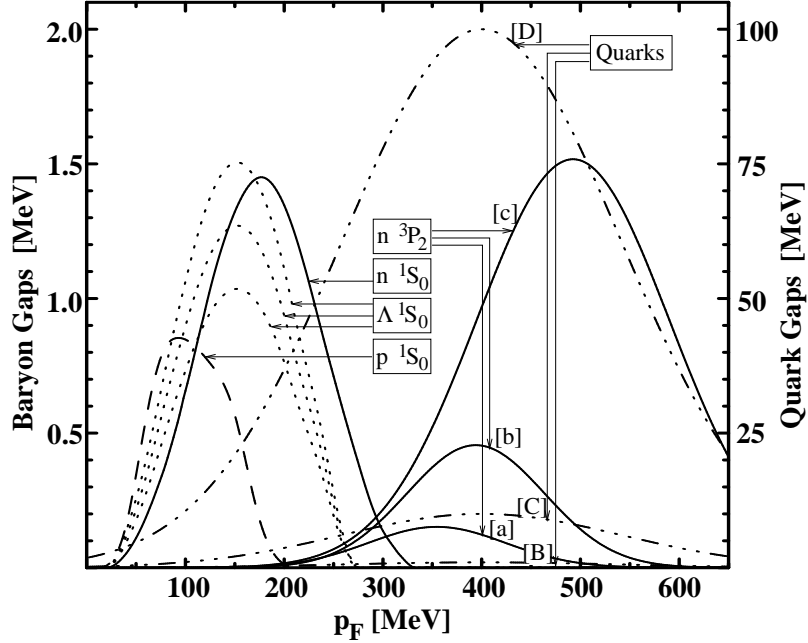


**Fig. 15.** Pairing gaps adopted for neutron  $^1S_0$  and  $^3P_2$ , proton  $^1S_0$ ,  $\Lambda$   $^1S_0$ , and quarks. The  $n$   $^3P_2$  gaps are anisotropic; plotted values are angle-averaged. The  $\Lambda$  gaps correspond, in order of increasing  $\Delta$ , to background densities  $n_B = 0.48, 0.64$  and  $0.8 \text{ fm}^{-3}$ , respectively. The s-wave quark gaps are schematic; see text for details

involving quarks, a mixed phase of baryons and quarks is constructed by satisfying Gibbs' phase rules for mechanical, chemical and thermal equilibrium [32]. The phase of pure quark matter exists only for very large baryon densities, and rarely occurs in our neutron star models. Baryonic matter is calculated using a field-theoretic model at the mean field level [87]; quark matter is calculated using either a bag-like model or the Nambu-Jona-Lasinio quark model [37,22]. The equation of state (EOS) is little affected by the pairing phenomenon, since the energy density gained is negligible compared to the ground state energy densities without pairing.

Additional particles, such as quarks or hyperons, have the effect of softening the EOS and increasing the central densities of stars relative to the  $np$  case. For the  $npQ$  model studied, a mixed phase appears at the density  $n_B = 0.48 \text{ fm}^{-3}$ . Although the volume fraction of quarks is initially zero, the quarks themselves have a significant  $p_F(q)$  when the phase appears. The  $p_F$ s of the three quark flavors become the same at extremely high density, but for the densities of interest they are different due to the presence of negatively charged leptons. In particular,  $p_F(s)$  is much smaller than  $p_F(u)$  and  $p_F(d)$  due to the larger s-quark mass. Use of the Nambu-Jona-Lasinio model, in which quarks acquire density-dependent masses resembling those of constituent quarks, exaggerates

the reduction of  $p_F(s)$ . This has dramatic consequences since the pairing phenomenon operates at its maximum strength when the Fermi momenta are exactly equal; even small asymmetries cause pairing gaps to be severely reduced [82,88]. In addition, one may also expect p-wave superfluidity, to date unexplored, which may yield gaps smaller than that for the s-wave. We therefore investigate pairing gaps that are much smaller than those reported for the case of s-wave superfluidity and equal quark  $p_F$ 's.

The introduction of hyperons does not change these generic trends. In the case  $npH$ , the appearance of hyperons changes the lepton and nucleon  $p_F$ 's similarly to the appearance of quarks although with less magnitude. While the appearance of quarks is delayed by the existence of hyperons, at high densities the  $p_F$ 's of nucleons and quarks remain similar to those of the  $npQ$  case. The existence of either hyperons or quarks, however, does allow the possibility of additional direct Urca processes involving themselves as well as those involving nucleons by decreasing  $p_F(n) - p_F(p)$ . For the  $npQ$  and  $npHQ$  models studied, the maximum masses are  $\cong 1.5M_\odot$ , the central baryon densities are  $\cong 1.35 \text{ fm}^{-3}$ , and the volume fractions of quarks at the center are  $\cong 0.4$ .

## 6.5 Examples of Results

Cooling simulations of stars without hyperons and with hyperons are compared, in Figs. 16 and 17, respectively, to available observations of thermal emissions from pulsars. Sources for the observational data can be found in [89]. However, at the present time, the inferred temperatures must be considered as upper limits because the total flux is contaminated, and in some cases dominated, by the pulsar's magnetospheric emission and/or the emission of a surrounding synchrotron nebula. Furthermore, the neutron star surface may be reheated by magnetospheric high energy photons and particles; late-time accretion for non-pulsing neutron stars is also possible. Other uncertainties arise in the temperature estimates due to the unknown chemical composition and magnetic field strength in the surface layers, and in the age, which is based upon the observed spin-down time. In these figures, the bolder the data symbol the better the data.

### $np$ and $npQ$ Matter

The  $np$  case is considered in Fig. 16, in which solid lines indicate the temperature evolution of a  $1.4 M_\odot$  star for quarkless matter: case [z] is for no nucleon pairing at all, and cases [a], [b] and [c] correspond to increasing values for the neutron  ${}^3P_2$  gap, according to Fig. 15. The field-theoretical model employed for the nucleon interactions allows the direct nucleon Urca process, which dominates the cooling. The unimpeded direct Urca process carries the temperature to values well below the inferred data. Pairing suppresses the cooling for  $T < T_c$ , where  $T$  is the interior temperature, so  $T_e$  increases with increasing  $\Delta$ . If the direct Urca process is not allowed, the range of predicted temperatures is relatively narrow due to the low emissivity of the modified Urca process. We show an example of

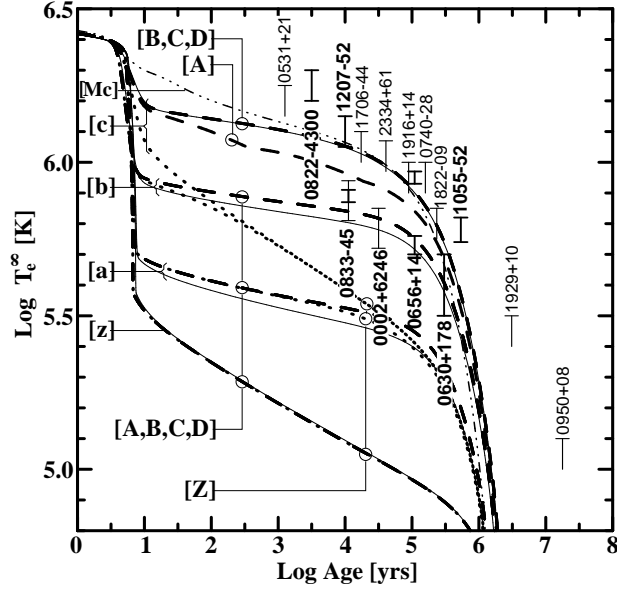


**Fig. 16.** Cooling of  $1.4M_{\odot}$  stars with  $np$  matter (continuous curves) and  $npQ$  matter (dashed and dotted curves). The curves labelled as [a], [b], and [c] correspond to  $n^3P_2$  gaps as in Fig. 15; [z] corresponds to zero  $n$  gap. Models labelled [A], [B], [C] and [D] correspond to quark gaps as in Fig. 15; [Z] corresponds to zero quark gap

such cooling (curve [Mc]) using the  $n^3P_2$  gap [c] for a  $1.4M_{\odot}$  with an EOS [90] for which the direct Urca cooling is not allowed.

The other curves in the figure illustrate the effects of quarks upon the cooling. The dotted curves [Z] are for vanishingly small quark gaps; the dashed curves ([A], [B], [C] and [D]) are for quark gaps as proposed in Fig. 15. For nonexistent ([z]) or small ([a]) nucleon gaps, the quark direct Urca process is irrelevant and the dependence on the existence or the size of the quark gaps is very small. However, for large nucleon gaps ([b] and [c]), the quark direct Urca process quickly dominates the cooling as the nucleon direct Urca process is quenched. It is clear that for quark gaps of order 1 MeV or greater ([B], [C] or [D]) the effect of quarks is again very small. There is at most a slight increase in the stars temperatures at ages between  $10^1$  to  $10^{5-6}$  years due to the reduction of  $p_F(n)$  and the consequent slightly larger gap (Fig. 15). Even if the quark gap is quite small ([A]), quarks have an effect only if the nucleon gap is very large ([b] or [c]), i.e., significantly larger than the quark gap: the nucleon direct Urca process is suppressed at high temperatures and the quark direct Urca process has a chance to contribute to the cooling. We find that the effects of changing the stellar mass  $M$  are similar to those produced by varying the baryon gap, so that only combinations of  $M$  and  $\Delta$  might be constrained by observation.



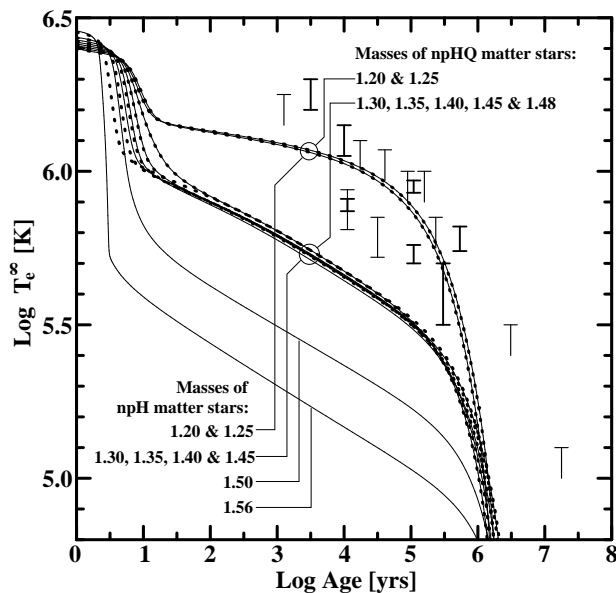


**Fig. 17.** Cooling of stars with  $npH$  (continuous lines) and  $npHQ$  matter (dotted lines) for various stellar masses (in  $M_\odot$ ).  $n^3P_2$  gaps are from case [c] while quark gaps, when present, are from model [C] of Fig. 15

### $npH$ and $npHQ$ Matter

The thermal evolution of stars containing hyperons has been discussed in [91,92], but we obtain qualitatively different results here. Hyperons open new direct Urca channels:  $\Lambda \rightarrow p + e + \bar{\nu}_e$  and  $\Lambda + e \rightarrow \Sigma^- + \nu_e$  if  $\Sigma^-$ 's are present, with their inverse processes. Previous results showed that the cooling is naturally controlled by the smaller of the  $\Lambda$  or  $n$  gap. However, this is significantly modified when the  $\Lambda$  gap is more accurately treated. At the  $\Lambda$  appearance threshold, the gap must vanish since  $p_F(\Lambda)$  is vanishingly small. We find that a very thin layer, only a few meters thick, of unpaired or weakly paired  $\Lambda$ 's is sufficient to control the cooling. This effect was overlooked in previous works perhaps because they lacked adequate zonal resolution.

In Fig. 17 we compare the evolution of stars of different masses made of either  $npH$  or  $npHQ$  matter. We find that all stars, except the most massive  $npH$  ones, follow two distinctive trajectories depending on whether their central density is below or above the threshold for  $\Lambda$  appearance ( $= 0.54 \text{ fm}^{-3}$  in our model EOS, the threshold star mass being  $1.28M_\odot$ ). In the case of  $npH$  matter, stars with  $M > 1.50M_\odot$  are dense enough so that the  $\Lambda^1S_0$  gap vanishes and hence undergo fast cooling, while stars made of  $npHQ$  matter do not attain such high densities. The temperatures of  $npH$  stars with masses between 1.3 and 1.5  $M_\odot$  are below the ones obtained in the models of Fig. 16 with the same  $n^3P_2$  gap [b], which confirms that the cooling is dominated by the very thin layer

of unpaired  $\Lambda$ 's (the slopes of these cooling curves are typical of direct Urca processes). Only if the  $n\ ^3P_2$  gap  $\lesssim 0.3$  MeV do the cooling curves fall below what is shown in Fig. 17. Notice, moreover, that in the mass range  $1.3 - 1.48 M_\odot$  the cooling curves are practically indistinguishable from those with unpaired quark matter shown in Fig. 16. In these models with  $npH$  or  $npHQ$  matter, there is almost no freedom to “fine-tune” the size of the gaps to attain a given  $T_e$ : stars with  $\Lambda$ 's will all follow the same cooling trajectory, determined by the existence of a layer of unpaired or weakly paired  $\Lambda$ 's, as long as the  $n\ ^3P_2$  gap is not smaller. It is, in some sense, the same result as in the case of  $np$  and  $npQ$  matter: the smallest gap controls the cooling and now the control depends on how fast the  $\Lambda\ ^1S_0$  gap increases with increasing  $p_F(\Lambda)$ .

## 6.6 Implications

Our results indicate that observations could constrain combinations of the smaller of the neutron and  $\Lambda$ -hyperon pairing gaps and the star's mass. Deducing the sizes of quark gaps from observations of neutron star cooling will be extremely difficult. Large quark gaps render quark matter practically invisible, while vanishing quark gaps lead to cooling behaviors which are nearly indistinguishable from those of stars containing nucleons or hyperons. Moreover, it also appears that cooling observations by themselves will not provide definitive evidence for the existence of quark matter itself.

## 7 The Structure of Catalyzed Stars

In this section, we explore from a theoretical perspective, how the structure of neutron star depends upon the assumed EOS. This study is crucial if new observations of masses and radii are to lead to effective constraints of the EOS of dense matter. Two general classes of stars can be identified: *normal* stars in which the density vanishes at the stellar surface, and *self-bound* stars in which the density at the surface is finite. Normal stars originate from nuclear force models which can be conveniently grouped into three broad categories: non-relativistic potential models, relativistic field theoretical models, and relativistic Dirac-Brueckner-Hartree-Fock models. In each of these approaches, the presence of additional softening components such as hyperons, Bose condensates or quark matter, can be incorporated. Details of these approaches have been further considered in Lattimer et al. [93] and Prakash et al. [4]. A representative sample, and some general attributes, including references and typical compositions, of equations of state employed here are summarized in Table 1.

For normal matter, the EOS is that of interacting nucleons above a transition density of  $1/3$  to  $1/2 n_s$ . Below this density, the ground state of matter consists of heavy nuclei in equilibrium with a neutron-rich, low-density gas of nucleons. However, for most of the purposes of this paper, the pressure in the region  $n < 0.1\ \text{fm}^{-3}$  is not relevant as it does not significantly affect the mass-radius relation or other global aspects of the star's structure. Nevertheless, the value

of the transition density, and the pressure there, are important ingredients for the determination of the size of the superfluid crust of a neutron star that is believed to be involved in the phenomenon of pulsar glitches (Link, Epstein, & Lattimer [94]).

Four equations of state are taken from Akmal & Pandharipande [11]. These are: AP1 (the AV18 potential), AP2 (the AV18 potential plus  $\delta v_b$  relativistic boost corrections), AP3 (the AV18 potential plus a three-body UIX potential), and AP4 (the AV18 potential plus the UIX potential plus the  $\delta v_b$  boost). Three equations of state from Müller & Serot [30], labelled MS1–3, correspond to different choices of the parameters  $\xi$  and  $\zeta$  which determine the strength of the nonlinear vector and isovector interactions at high densities. The numerical values used are  $\xi = \zeta = 0$ ;  $\xi = 1.5, \zeta = 0.06$ ; and  $\xi = 1.5, \zeta = 0.02$ , respectively. Six EOSs come from the phenomenological non-relativistic potential model of Prakash, Ainsworth & Lattimer [95], labelled PAL1–6, which have different choices of the symmetry energy parameter at the saturation density, its density dependence, and the bulk nuclear matter incompressibility parameter  $K_s$ . The incompressibilities of PAL1–5 were chosen to be  $K_s = 180$  or  $240$  MeV, but PAL6 has  $K_s = 120$  MeV. Three interactions denoted GM1–3 come from the field-theoretical model of Glendenning & Moszkowski [13]. Two interactions come from the field-theoretical model of Glendenning & Schaffner-Bielich [15]: GL78 with  $U_K(\rho_0) = -140$  MeV and TM1 with  $U_K = -185$  MeV. The labels denoting the other EOSs in Table 1 are identical to those in the original references.

The rationale for exploring a wide variety of EOSs, even some that are relatively outdated or in which systematic improvements are performed, is two-fold. First, it provides contrasts among widely different theoretical paradigms. Second, it illuminates general relationships that exist between the pressure-density relation and the macroscopic properties of the star such as the radius. For example, AP4 represents the most complete study to date of Akmal & Pandharipande [11], in which many-body and special relativistic corrections are progressively incorporated into prior models, AP1–3. AP1–3 are included here because they represent different pressure-energy density-baryon density relations, and serve to reinforce correlations between neutron star structure and microscopic physics observed using alternative theoretical paradigms. Similarly, several different parameter sets for other EOSs are chosen.

In all cases, except for PS (Pandharipande & Smith [97]), the pressure is evaluated assuming zero temperature and beta equilibrium without trapped neutrinos. PS only contains neutrons among the baryons, there being no charged components. We chose to include this EOS, despite the fact that it has been superseded by more sophisticated calculations by Pandharipande and coworkers, because it represents an extreme case producing large radii neutron stars.

The pressure-density relations for some of the selected EOSs are shown in Fig. 18 which displays three significant features to note for normal EOSs. First, there is a fairly wide range of predicted pressures for beta-stable matter in the density domain  $n_s/2 < n < 2n_s$ . For the EOSs displayed, the range of pressures

**Table 1.** Approach refers to the underlying theoretical technique. Composition refers to strongly interacting components (n=neutron, p=proton, H=hyperon, K=kaon, Q=quark); all models include leptonic contributions.

Symbol	Reference	Approach	Composition
FP	Friedman & Pandharipande [96]	Variational	np
PS	Pandharipande & Smith [97]	Potential	$n\pi^0$
WFF(1-3)	Wiringa, Fiks & Fabrocine [98]	Variational	np
AP(1-4)	Akmal & Pandharipande [11]	Variational	np
MS(1-3)	Müller & Serot [30]	Field Theoretical	np
MPA(1-2)	Müther, Prakash & Ainsworth [99]	Dirac-Brueckner HF	np
ENG	Engvik et al. [100]	Dirac-Brueckner HF	np
PAL(1-6)	Prakash, Ainsworth & Lattimer [95]	Schematic Potential	np
GM(1-3)	Glendenning & Moszkowski [13]	Field Theoretical	npH
GS(1-2)	Glendenning & Schaffner-Bielich [34]	Field Theoretical	npK
PCL(1-2)	Prakash, Cooke & Lattimer [37]	Field Theoretical	npHQ
SQM(1-3)	Prakash, Cooke & Lattimer [37]	Quark Matter	$Q(u, d, s)$

covers about a factor of five, but this survey is by no means exhaustive. That such a wide range in pressures is found is somewhat surprising, given that each of the EOSs provides acceptable fits to experimentally-determined nuclear matter properties. Clearly, the extrapolation of the pressure from symmetric matter to nearly pure neutron matter is poorly constrained. Second, the *slopes* of the pressure curves are rather similar. A polytropic index of  $n \simeq 1$ , where  $P = Kn^{1+1/n}$ , is implied. Third, in the density domain below  $2n_s$ , the pressure-density relations seem to fall into two groups. The higher pressure group is primarily composed of relativistic field-theoretical models, while the lower pressure group is primarily composed of non-relativistic potential models. It is significant that relativistic field-theoretical models generally have symmetry energies that increase proportionately to the density while potential models have much less steeply rising symmetry energies.

A few of the plotted normal EOSs have considerable softening at high densities, especially PAL6, GS1, GS2, GM3, PS and PCL2. PAL6 has an abnormally small value of incompressibility ( $K_s = 120$  MeV). GS1 and GS2 have phase transitions to matter containing a kaon condensate, GM3 has a large population of hyperons appearing at high density, PS has a phase transition to a neutral pion condensate and a neutron solid, and PCL2 has a phase transition to a mixed phase containing strange quark matter. These examples are representative of the kinds of softening that could occur at high densities.

The best-known example of self-bound stars results from Witten's [101] conjecture (also see Fahri & Jaffe [102], Haensel, Zdunik & Schaeffer [103], Alcock & Olinto [104], and Prakash et al. [105]) that strange quark matter is the ultimate ground state of matter. In this paper, the self-bound EOSs are represented by strange-quark matter models SQM1–3, using perturbative QCD and an MIT-type bag model, with parameter values given in Table 2. The existence of an energy ceiling equal to the baryon mass, 939 MeV, for zero pressure matter

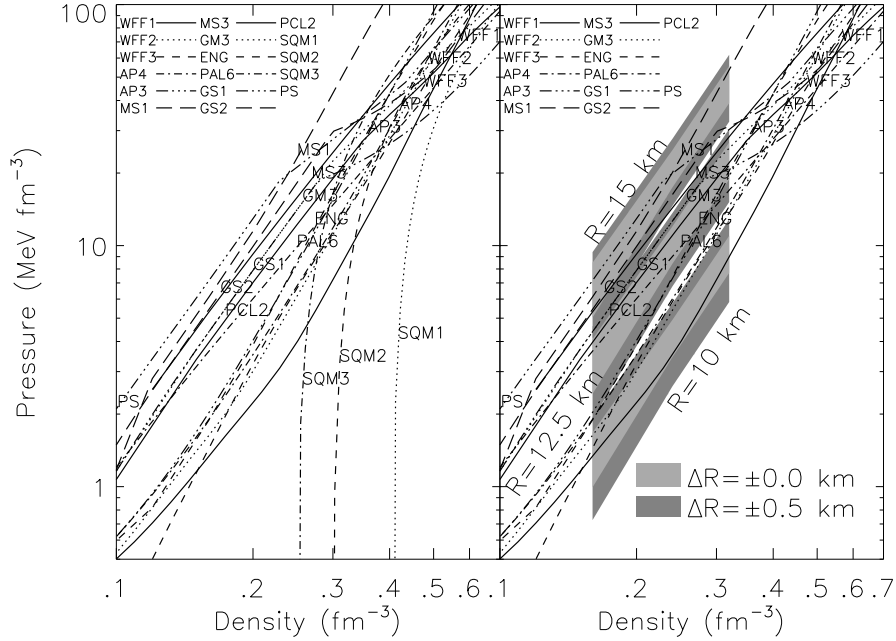


**Fig. 18.** Left: The pressure-density relation for a selected set of EOSs contained in Table 1. The pressure is in units of  $\text{MeV fm}^{-3}$  and the density is in units of baryons per cubic fermi. The nuclear saturation density is approximately  $0.16 \text{ fm}^{-3}$ . Right: The pressures inferred from the empirical correlation Eq. (65), for three hypothetical radius values (10, 12.5 and 15 km) overlaid on the pressure-density relations shown on the left. The light shaded region takes into account only the uncertainty associated with  $C(n, M)$ ; the dark shaded region also includes a hypothetical uncertainty of 0.5 km in the radius measurement. The neutron star mass was assumed to be  $1.4 M_{\odot}$ .

requires that the bag constant  $B \leq 94.92 \text{ MeV fm}^{-3}$ . This limiting value is chosen, together with zero strange quark mass and no interactions ( $\alpha_c = 0$ ), for the model SQM1. The other two models chosen, SQM2 and SQM3, have bag constants adjusted so that their energy ceilings are also 939 MeV.

**Table 2.** Parameters for self-bound strange quark stars. Numerical values employed in the MIT bag model as described in Fahri & Jaffe [102].

Model	$B$ ( $\text{MeV fm}^{-3}$ )	$m_s$ (MeV)	$\alpha_c$
SQM1	94.92	0	0
SQM2	64.21	150	0.3
SQM3	57.39	50	0.6

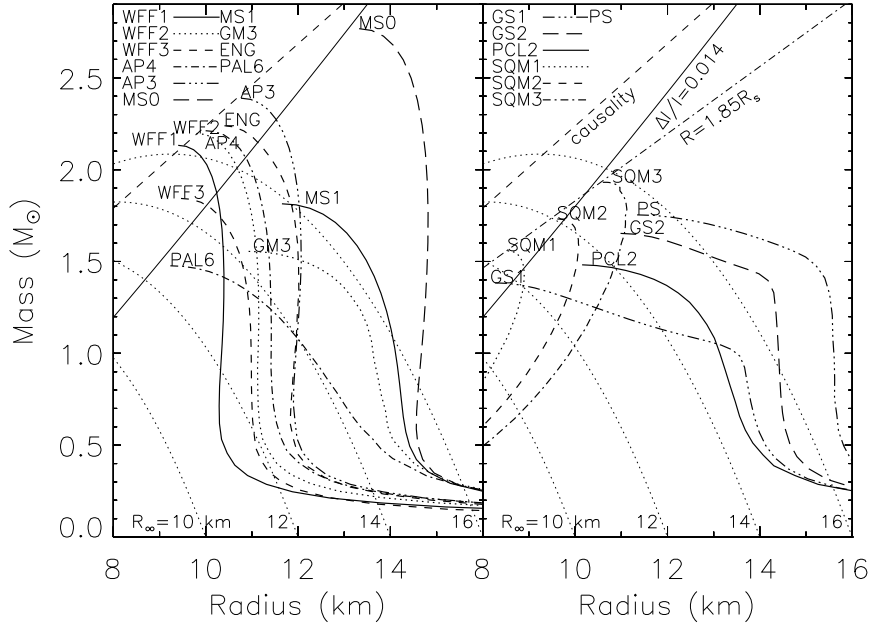
## 7.1 Neutron Star Radii

Fig. 19 displays the resulting mass-radius relations for catalyzed matter. Rhoades & Ruffini [106] demonstrated that the assumption of causality beyond a fiducial density  $\rho_f$  sets an upper limit to the maximum mass of a neutron star:  $4.2\sqrt{\rho_s/\rho_f} M_\odot$ . Lattimer et al. [93] have shown that the causality constraint also sets a lower limit to the radius:  $R \gtrsim 1.52R_s$ , where  $R_s = 2GM/c^2$ , which is shown in Fig. 19. For a  $1.4 M_\odot$  star, this is about 4.5 km. The most reliable estimates of neutron star radii in the near future will likely stem from observations of thermal emission from their surfaces. Such estimates yield the so-called “radiation radius”  $R_\infty = R/\sqrt{1 - R_s/R}$ , a quantity resulting from redshifting the star’s luminosity and temperature. A given value of  $R_\infty$  implies that  $R < R_\infty$  and  $M < 0.13(R_\infty/\text{km}) M_\odot$ . Contours of  $R_\infty$  are also displayed. With the exception of model GS1, the EOSs used to generate Fig. 19 result in maximum masses greater than  $1.442 M_\odot$ , the limit obtained from PSR 1913+16. From a theoretical perspective, it appears that values of  $R_\infty$  in the range of 12–20 km are possible for normal neutron stars whose masses are greater than  $1 M_\odot$ .

One observes that *normal* neutron stars have minimum masses of about  $0.1 M_\odot$  that are primarily determined by the EOS below  $n_s$ . At the minimum mass, the radii are generally in excess of 100 km. Self-bound stars have no minimum mass and the maximum mass self-bound stars have nearly the largest radii possible for a given EOS. If the strange quark mass  $m_s = 0$  and interactions are neglected ( $\alpha_c = 0$ ), the maximum mass is related to the bag constant  $B$  in the MIT-type bag model by  $M_{max} = 2.033 (56 \text{ MeV fm}^{-3}/B)^{1/2} M_\odot$ . Prakash et al. [105] and Lattimer et al. [93] showed that the addition of a finite strange quark mass and/or interactions produces larger maximum masses. The constraint that  $M_{max} > 1.44 M_\odot$  is thus automatically satisfied by the condition that the energy ceiling is 939 MeV, and non-zero values of  $m_s$  and  $\alpha_c$  yield larger radii for every mass. The locus of maximum masses is given simply by  $R \cong 1.85R_s$  (Lattimer et al. [93]) as shown in the right-hand panel of Fig. 19. Strange quark stars with electrostatically supported normal-matter crusts (Glendenning & Weber [107]) have larger radii than those with bare surfaces. Coupled with the additional constraint  $M > 1M_\odot$  from protoneutron star models, MIT-model strange quark stars cannot have  $R < 8.5$  km or  $R_\infty < 10.5$  km. These values are comparable to the smallest possible radii for a Bose (pion or kaon) condensate EOS.

One striking feature of Fig. 19 is that in the mass range from 1–1.5  $M_\odot$  or more the radius has relatively little dependence upon the stellar mass. The major exceptions illustrated are the model GS1, in which a mixed phase containing a kaon condensate appears at a relatively low density, and the model PAL6, which has an extremely small nuclear incompressibility (120 MeV). Both of these have considerable softening and a large increase in central density for  $M > 1 M_\odot$ .

While it is generally assumed that a stiff EOS implies both a large maximum mass and a large radius, many counter examples exist. For example, GM3, MS1 and PS have relatively small maximum masses but have large radii compared to most other EOSs with larger maximum masses. Also, not all EOSs with extreme softening have small radii for  $M > 1 M_\odot$  (e.g., GS2, PS). Nonetheless, for stars



**Fig. 19.** Mass-radius curves for several EOSs listed in Table 1. The left panel is for stars containing nucleons and, in some cases, hyperons. The right panel is for stars containing more exotic components, such as mixed phases with kaon condensates or strange quark matter, or pure strange quark matter. In both panels, the lower limit causality places on  $R$  is shown as a dashed line, a constraint derived from glitches in the Vela pulsar is shown as the solid line labelled  $\Delta I/I = 0.014$ , and contours of constant  $R_\infty = R/\sqrt{1 - 2GM/Rc^2}$  are shown as dotted curves. In the right panel, the theoretical trajectory of maximum masses and radii for pure strange quark matter stars is marked by the dot-dash curve labelled  $R = 1.85R_s$ .

with masses greater than  $1 M_\odot$ , only models with a large degree of softening (including strange quark matter configurations) can have  $R_\infty < 12$  km.

To understand the relative insensitivity of the radius to the mass for normal neutron stars, it is relevant that a Newtonian polytrope with  $n = 1$  has the property that the stellar radius is independent of both the mass and central density. An  $n = 1$  polytrope also has the property that the radius is proportional to the square root of the constant  $K$  in the polytropic pressure law  $P = K\rho^{1+1/n}$ . This suggests that there might be a quantitative relation between the radius and the pressure that does not depend upon the EOS at the highest densities, which determines the overall softness or stiffness (and hence, the maximum mass).

In fact, this conjecture may be verified. Fig. 20 shows a remarkable empirical correlation between the radii of  $1$  and  $1.4 M_\odot$  normal stars and the matter's

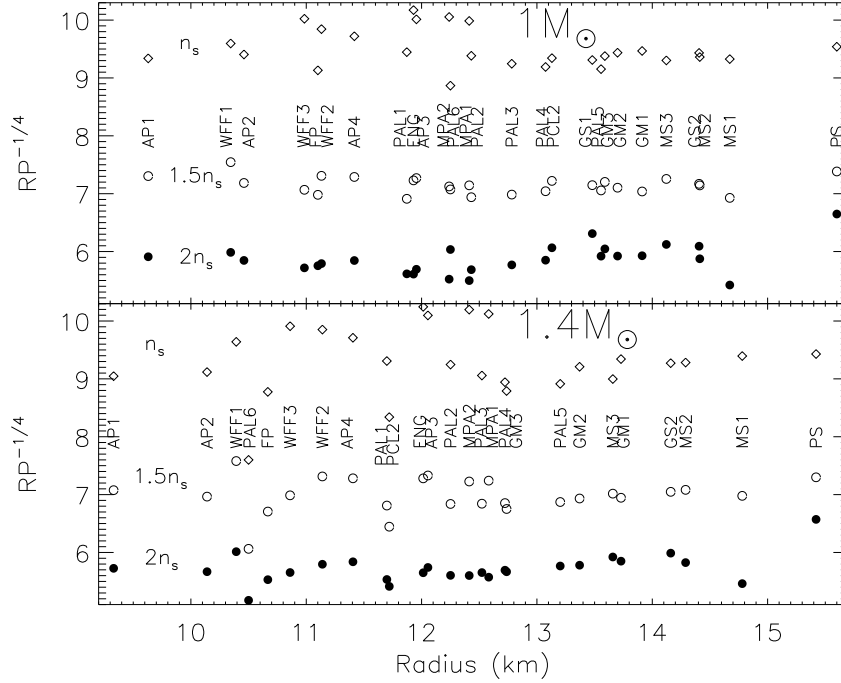


**Fig. 20.** Empirical relation between pressure, in units of  $\text{MeV fm}^{-3}$ , and  $R$ , in km, for EOSs listed in Table 1. The upper panel shows results for  $1 M_{\odot}$  (gravitational mass) stars; the lower panel is for  $1.4 M_{\odot}$  stars. The different symbols show values of  $RP^{-1/4}$  evaluated at three fiducial densities

pressure evaluated at fiducial densities of 1, 1.5 and  $2 n_s$ . Numerically, the correlation has the form of a power law between the radius  $R_M$ , defined as the radius at a particular mass  $M$ , and the total pressure  $P(n)$  evaluated at a given density:

$$R_M \simeq C(n, M) [P(n)]^{0.23-0.26}. \quad (65)$$

$C(n, M)$  is a number that depends on the density  $n$  at which the pressure was evaluated and the stellar mass  $M$ . An exponent of 1/4 was chosen for display in Fig. 20, but the correlation holds for a small range of exponents about this value. Using an exponent of 1/4, and ignoring points associated with EOSs with phase transitions in the density ranges of interest, we find values for  $C(n, M)$ , in units of  $\text{km fm}^{3/4} \text{MeV}^{-1/4}$ , which are listed in Table 3. The error bars are taken from the standard deviations. The correlation is seen to be somewhat tighter for the baryon density  $n = 1.5n_s$  and  $2n_s$  cases. Despite the relative insensitivity of radius to mass for a particular EOS in this mass range, the nominal radius  $R_M$  has a variation  $\sim 5$  km. The largest deviations from this correlation occur for EOSs with extreme softening or for configurations very near their maximum mass. This correlation is valid only for cold, catalyzed neutron stars, i.e., not



for protoneutron stars which have finite entropies and might contain trapped neutrinos.

**Table 3.** The quantity  $C(n, M)$  of Eq. (65) The quantity  $C(n, M)$ , in units of  $\text{km fm}^{3/4} \text{MeV}^{-1/4}$ , which relates the pressure (evaluated at density  $n$ ) to the radius of neutron stars of mass  $M$ . The errors are standard deviations

$n$	$1 M_\odot$	$1.4 M_\odot$
$n_s$	$9.53 \pm 0.32$	$9.30 \pm 0.60$
$1.5n_s$	$7.14 \pm 0.15$	$7.00 \pm 0.31$
$2n_s$	$5.82 \pm 0.21$	$5.72 \pm 0.25$

If a measurement of  $P$  near  $n_s$  can be deduced in this way, an important clue about the symmetry properties of matter will be revealed. The energy per particle and pressure of cold, beta stable nucleonic matter is

$$\begin{aligned} E(n, x) &\simeq E(n, 1/2) + S_v(n)(1 - 2x)^2, \\ P(n, x) &\simeq n^2[E'(n, 1/2) + S'_v(n)(1 - 2x)^2], \end{aligned} \quad (66)$$

where  $E(n, 1/2)$  is the energy per particle of symmetric matter and  $S_v(n)$  is the bulk symmetry energy (which is density dependent). Primes denote derivatives with respect to density. If only one term in this expansion is important, as noted by Prakash, Ainsworth & Lattimer [95], then

$$S_v(n) \simeq \frac{1}{2} \frac{\partial^2 E(n, x)}{\partial x^2} \simeq E(n, 0) - E(n, 1/2). \quad (67)$$

At  $n_s$ , the symmetry energy can be estimated from nuclear mass systematics and has the value  $S_v \equiv S_v(n_s) \approx 27 - 36$  MeV. Attempts to further restrict this range from consideration of fission barriers and the energies of giant resonances provide constraints between  $S_v$  and  $S_v(n)$  primarily by providing correlations between  $S_v$  and  $S_s$ , the surface symmetry parameter. Lattimer & Prakash [108] detail how  $S_s$  is basically a volume integral of the quantity  $1 - S_v/S_v(n)$  through the nucleus. However, both the magnitude of  $S_v$  and its density dependence  $S_v(n)$  remain uncertain. Part of the bulk symmetry energy is due to the kinetic energy for noninteracting matter, which for degenerate nucleonic matter is proportional to  $n^{2/3}$ , but the remainder of the symmetry energy, due to interactions, is also expected to contribute significantly to the overall density dependence.

Leptonic contributions must be added to Eq. (66) to obtain the total energy and pressure; the electron energy per baryon is  $(3/4)\hbar c x(3\pi^2 n x)^{1/3}$ . Matter in neutron stars is in beta equilibrium, i.e.,  $\mu_e = \mu_n - \mu_p = -\partial E/\partial x$ , which permits the evaluation of the equilibrium proton fraction. The pressure at the saturation density becomes

$$P_s = n_s(1 - 2x_s)[n_s S'_v(1 - 2x_s) + S_v x_s], \quad (68)$$

where  $S'_v \equiv S'_v(n_s)$  and the equilibrium proton fraction at  $n_s$  is

$$x_s \simeq (3\pi^2 n_s)^{-1} (4S_v/\hbar c)^3 \simeq 0.04, \quad (69)$$

for  $S_v = 30$  MeV. Due to the small value of  $x_s$ , we find that  $P_s \simeq n_s^2 S'_v$ .

Were we to evaluate the pressure at a larger density, contributions featuring other nuclear parameters, including the nuclear incompressibility  $K_s = 9(dP/dn)|_{n_s}$  and the skewness  $K'_s = -27n_s^3(d^3E/dn^3)|_{n_s}$ , also contribute. However, the  $K_s$  and  $K'_s$  terms largely cancel, up to  $2n_s$ , so the symmetry term dominates.

At present, experimental guidance concerning the density dependence of the symmetry energy is limited and mostly based upon the division of the nuclear symmetry energy between volume and surface contributions. Upcoming experiments involving heavy-ion collisions which might sample densities up to  $\sim (3-4)n_s$ , will be limited to analyzing properties of the nearly symmetric nuclear matter EOS through a study of matter, momentum, and energy flow of nucleons. However, the parity-violating experiment [109] to accurately determine the thickness of the neutron skin in  $^{208}\text{Pb}$  at Jefferson Lab will provide important constraints. The neutron skin thickness is directly proportional to  $S_s/S_v$ . In addition, studies of heavy nuclei far off the neutron drip lines using radioactive ion beams might also provide useful constraints.

## 7.2 Moments of Inertia

Besides the stellar radius, other global attributes of neutron stars are potentially observable, including the moment of inertia and the binding energy. These quantities depend primarily upon the ratio  $M/R$  as opposed to details of the EOS (Lattimer & Prakash [5]).

The moment of inertia, for a star uniformly rotating with angular velocity  $\Omega$ , is

$$I = (8\pi/3) \int_0^R r^4 (\rho + P/c^2) e^{(\lambda-\nu)/2} (\omega/\Omega) dr. \quad (70)$$

The metric function  $\omega(r)$  is a solution of the equation

$$d[r^4 e^{-(\lambda+\nu)/2} \omega']/dr + 4r^3 \omega de^{-(\lambda+\nu)/2}/dr = 0 \quad (71)$$

with the surface boundary condition

$$\omega_R = \Omega - \frac{R}{3} \omega'_R = \Omega \left[ 1 - \frac{2GI}{R^3 c^2} \right]. \quad (72)$$

The second equality in the above follows from the definition of  $I$  and the TOV equation. Writing  $j = \exp[-(\nu + \lambda)/2]$ , the TOV equation becomes

$$j' = -4\pi G r (P/c^2 + \rho) j e^\lambda / c^2. \quad (73)$$

Then, one has

$$I = -\frac{2c^2}{3G} \int \frac{\omega}{\Omega} r^3 dj = \frac{c^2 R^4 \omega'_R}{6G\Omega}. \quad (74)$$

Useful approximations which are valid for three analytic, exact, solutions to GR, the incompressible fluid (Inc), the Tolman VII (Tolman [110]; VII) solution, and Buchdahl's [111] solution (Buch), are

$$I_{Inc}/MR^2 \simeq 2(1 - 0.87\beta - 0.3\beta^2)^{-1}/5, \quad (75)$$

$$I_{Buch}/MR^2 \simeq (2/3 - 4/\pi^2)(1 - 1.81\beta + 0.47\beta^2)^{-1}, \quad (76)$$

$$I_{TVII}/MR^2 \simeq 2(1 - 1.1\beta - 0.6\beta^2)^{-1}/7. \quad (77)$$

Fig. 21 indicates that the T VII approximation is a rather good approximation to most EOSs without extreme softening at high densities, for  $M/R \geq 0.1 M_\odot/\text{km}$ . The EOSs with softening fall below this trajectory.

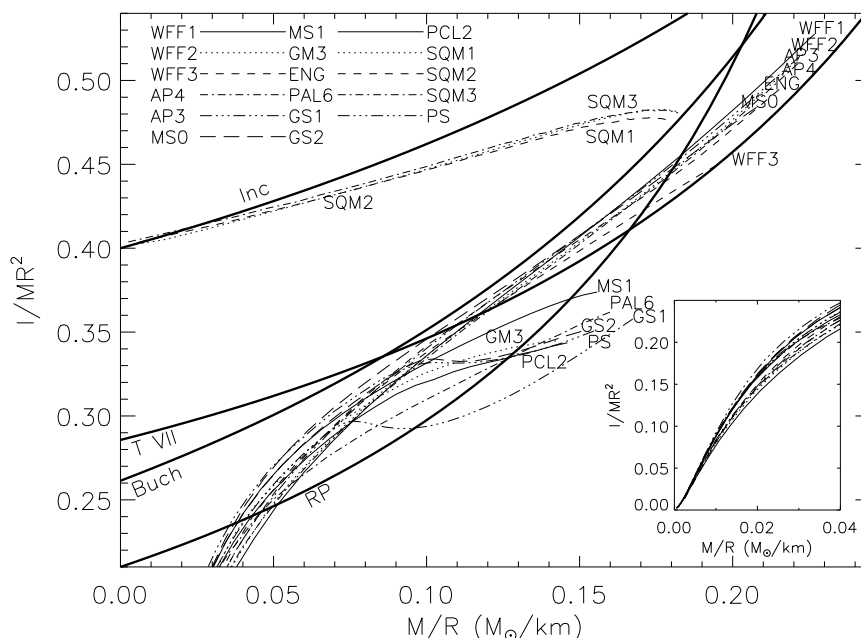


**Fig. 21.** The moment of inertia  $I$ , in units of  $MR^2$ , for several EOSs listed in Table 1. The curves labelled “Inc”, “T VII”, “Buch” and “RP” are for an incompressible fluid, the Tolman [110] VII solution, the Buchdahl [111] solution, and an approximation of Ravenhall & Pethick [112], respectively. The inset shows details of  $I/MR^2$  for  $M/R \rightarrow 0$

Another interesting result from Fig. 21 concerns the moments of inertia of strange quark matter stars. Such stars are relatively closely approximated by incompressible fluids, this behavior becoming exact in the limit of  $\beta \rightarrow 0$ . This could have been anticipated from the  $M \propto R^3$  behavior of the  $M - R$  trajectories for small  $\beta$  strange quark matter stars as observed in Fig. 19.

### 7.3 Crustal Fraction of the Moment of Inertia

A new observational constraint involving  $I$  concerns pulsar glitches. Occasionally, the spin rate of a pulsar will suddenly increase (by about a part in  $10^6$ ) without warning after years of almost perfectly predictable behavior. However, Link, Epstein & Lattimer [94] argue that these glitches are not completely random: the Vela pulsar experiences a sudden spinup about every three years, before returning to its normal rate of slowing. Also, the size of a glitch seems correlated with the interval since the previous glitch, indicating that they represent self-regulating instabilities for which the star prepares over a waiting time. The angular momentum requirements of glitches in Vela imply that  $\geq 1.4\%$  of the star's moment of inertia drives these events.

Glitches are thought to represent angular momentum transfer between the crust and another component of the star. In this picture, as a neutron star's crust spins down under magnetic torque, differential rotation develops between the stellar crust and this component. The more rapidly rotating component then acts as an angular momentum reservoir which occasionally exerts a spin-up torque on the crust as a consequence of an instability. A popular notion at present is that the freely spinning component is a superfluid flowing through a rigid matrix in the thin crust, the region in which dripped neutrons coexist with nuclei, of the star. As the solid portion is slowed by electromagnetic forces, the liquid continues to rotate at a constant speed, just as superfluid He continues to spin long after its container has stopped. This superfluid is usually assumed to locate in the star's crust, which thus must contain at least 1.4% of the star's moment of inertia.

The high-density boundary of the crust is naturally set by the phase boundary between nuclei and uniform matter, where the pressure is  $P_t$  and the density  $n_t$ . The low-density boundary is the neutron drip density, or for all practical purposes, simply the star's surface since the amount of mass between the neutron drip point and the surface is negligible. One can utilize Eq. (70) to determine the moment of inertia of the crust alone with the assumptions that  $P/c^2 \ll \rho$ ,  $m(r) \simeq M$ , and  $\omega_j \simeq \omega_R$  and  $P \propto \rho^{4/3}$  in the crust (Lattimer & Prakash [5]:

$$\frac{\Delta I}{I} \simeq \frac{28\pi P_t R^3}{3Mc^2} \frac{(1 - 1.67\beta - 0.6\beta^2)}{\beta} \left[ 1 + \frac{2P_t(1 + 5\beta - 14\beta^2)}{n_t m_b c^2 \beta^2} \right]^{-1}. \quad (78)$$

In general, the EOS parameter  $P_t$ , in the units of MeV fm<sup>-3</sup>, varies over the range  $0.25 < P_t < 0.65$  for realistic EOSs. The determination of this parameter requires a calculation of the structure of matter containing nuclei just below nuclear matter density that is consistent with the assumed nuclear matter EOS. Unfortunately, few such calculations have been performed. Like the fiducial pressure at and above nuclear density which appears in Eq. (65),  $P_t$  should depend sensitively upon the behavior of the symmetry energy near nuclear density.

Link, Epstein & Lattimer [94] established a lower limit to the radius of the Vela pulsar by using Eq. (78) with  $P_t$  at its maximum value and the glitch

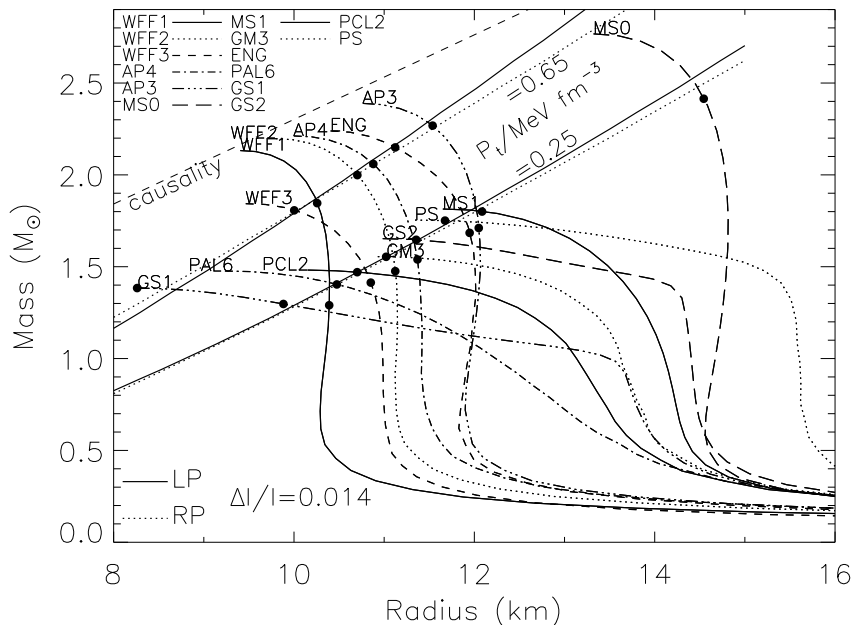


**Fig. 22.** Mass-radius curves for selected EOSs from Table 1, comparing theoretical contours of  $\Delta I/I = 0.014$  from approximations developed in this paper, labelled “LP”, and from Ravenhall & Pethick [112], labelled “RP”, to numerical results (solid dots). Two values of  $P_t$ , the transition pressure demarking the crust’s inner boundary, which bracket estimates in the literature, are employed. The region to the left of the  $P_t = 0.65$  MeV fm $^{-3}$  curve is forbidden if Vela glitches are due to angular momentum transfers between the crust and core, as discussed in Link, Epstein & Lattimer [94]. For comparison, the region excluded by causality alone lies to the left of the dashed curve labelled “causality” as determined by Lattimer et al. [93] and Glendenning [113]

constraint  $\Delta I/I \geq 0.014$ :

$$R > 3.9 + 3.5M/M_\odot - 0.08(M/M_\odot)^2 \text{ km}. \quad (79)$$

As shown in Fig. 22, this constraint is somewhat more stringent than one based upon causality. Better estimates of the maximum value of  $P_t$  should make this constraint more stringent.

#### 7.4 Binding Energies

The binding energy formally represents the energy gained by assembling  $N$  baryons. If the baryon mass is  $m_b$ , the binding energy is simply  $BE = Nm_b - M$  in mass units. However, the quantity  $m_b$  has various interpretations in the literature. Some authors take it to be 939 MeV/ $c^2$ , the same as the neutron or proton mass. Others take it to be about 930 MeV/ $c^2$ , corresponding to the mass of C $^{12}/12$  or Fe $^{56}/56$ . The latter choice would be more appropriate if  $BE$  was to

represent the energy released in by the collapse of a white-dwarf-like iron core in a supernova explosion. The difference in these definitions, 10 MeV per baryon, corresponds to a shift of  $10/939 \simeq 0.01$  in the value of  $BE/M$ . This energy,  $BE$ , can be deduced from neutrinos detected from a supernova event; indeed, it might be the most precisely determined aspect of the neutrino signal.

Lattimer & Yahil [114] suggested that the binding energy could be approximated as

$$BE \approx 1.5 \cdot 10^{51} (M/M_\odot)^2 \text{ ergs} = 0.084 (M/M_\odot)^2 M_\odot. \quad (80)$$

Prakash et al. [4] also concluded that such a formula was a reasonable approximation, based upon a comparison of selected non-relativistic potential and field-theoretical models, good to about  $\pm 20\%$ .

However, Lattimer & Prakash [5] proposed a more accurate representation of the binding energy:

$$BE/M \simeq 0.6\beta/(1 - 0.5\beta), \quad (81)$$

which incorporates some radius dependence. Thus, the observation of supernova neutrinos, and the estimate of the total radiated neutrino energy, will yield more accurate information about  $M/R$  than about  $M$  alone.

## 7.5 Outlook for Radius Determinations

Any measurement of a radius will have some intrinsic uncertainty. In addition, the empirical relation we have determined between the pressure and radius has a small uncertainty. It is useful to display how accurately the equation of state might be established from an eventual radius measurement. This can be done by inverting Eq. (65), which yields

$$P(n) \simeq [R_M/C(n, M)]^4. \quad (82)$$

The inferred ranges of pressures, as a function of density and for three possible values of  $R_{1.4}$ , are shown in the right panel of Fig. 18. It is assumed that the mass is  $1.4 M_\odot$ , but the results are relatively insensitive to the actual mass. Note from Table 3 that the differences between  $C$  for 1 and  $1.4 M_\odot$  are typically less than the errors in  $C$  itself. The light shaded areas show the pressures including only errors associated with  $C$ . The dark shaded areas show the pressures when a hypothetical observational error of 0.5 km is also taken into account. These results suggest that a useful restriction to the equation of state is possible if the radius of a neutron star can be measured to an accuracy better than about 1 km.

The reason useful constraints might be obtained from just a single measurement of a neutron star radius, rather than requiring a series of simultaneous mass-radii measurements as Lindblom [115] proposed, stems from the fact that we have been able to establish the empirical correlation, Eq. (65). In turn, it appears that this correlation exists because most equations of state have slopes  $d \ln P/d \ln n \simeq 2$  near  $n_s$ .

## 8 Tasks and Prospects

There are several topics that will merit attention from theoretical and experimental perspectives. Among those dealing with  $\nu$ -matter interactions are:

### Dynamic Structure Functions from Microscopic Calculations

Neutrino properties of astrophysical interest depend crucially on the nature of the excitation spectrum of the nuclear medium to spin and spin-isospin probes. The excited states are very different depending upon whether or not interactions in the medium conserve spin and spin-isospin. The importance of tensor correlations in the medium is thus clear, since they break the conservation laws. Friman & Maxwell [116] first emphasized the importance of tensor correlations in the process

$$\nu_e + n + n \rightarrow e^- + p + n, \quad (83)$$

and noted that their neglect underestimates the rate of  $\nu_e$  absorption by as much as an order of magnitude. In their study, they used a hard core description of the short range correlations and a one pion exchange model for the medium and long range ones. Sawyer & Soni [117] and Haensel & Jerzak [118], who used additional correlations based on a Reid soft core potential, confirmed that large reductions were possible in degenerate matter for non-degenerate neutrinos.

Since these earlier works, many-body calculations have vastly improved (e.g. [11]) and have been well-tested against data on light nuclei and nuclear matter. Much better tensor correlations are now available, so that we may better pin down the rate of absorption due to the above process. Detailed calculations to include arbitrary matter and neutrino degeneracies encountered in many astrophysical applications are necessary.

### Axial Charge Renormalization

In dense matter, the axial charge of the baryons is renormalized [119,120,121], which alters the neutrino-baryon couplings from their vacuum values. Since the axial contribution to the scattering and absorption reactions is typically three times larger than the vector contributions, small changes in the axial vector coupling constants significantly affect the cross sections. The calculation of this renormalization requires a theoretical approach which treats the pion and chiral symmetry breaking explicitly. So far, this has been done in isospin symmetric nuclear matter [122], but not for neutron matter or for beta-equilibrated neutron star matter. Substantial reductions may be expected in the  $\nu$ -matter cross sections from this in-medium effect.

### Multi-Pair Excitations

Neutrinos can also excite many-particle states in an interacting system, inverse bremsstrahlung being an example of a two-particle excitation [123]. These excitations provide an efficient means of transferring energy between the neutrinos and

baryons which are potentially significant in low-density matter. However, multi-group neutrino transport will be needed to include this effect. In addition, such calculations require source terms for neutrino processes such as bremsstrahlung and neutrino pair production. The latter process has been accurately treated in [124].

### $\pi^-$ and $K^-$ Dispersion Relations Through $\nu$ -Nucleus Reactions

The experimental program that would do the most to illuminate theoretical issues permeating neutrino interactions in dense matter would be studies of neutrino reactions on heavy nuclei, the only direct way of probing the matrix elements of the axial current in nuclear matter. Pioneering suggestions in this regard have been put forth by Sawyer & Soni [125,126], Ericson [127], and Sawyer [128]. The basic idea is to detect positively charged leptons ( $\mu^+$  or  $e^+$ ) produced in inclusive experiments

$$\bar{\nu} + X \rightarrow \mu^+ \text{ ( or } e^+ \text{ )} + \pi^- \text{ ( or } K^- \text{ )} + X \quad (84)$$

which is kinematically made possible when the in-medium  $\pi^-$  or  $K^-$  dispersion relation finds support in space-like regions. The sharp peaks at forward angles in the differential cross section versus lepton momentum survive the 100-200 MeV width in the incoming GeV or so neutrinos from accelerator experiments. Calculations of the background from quasi-elastic reactions indicate that the signal would be easily detectable.

### $\nu$ -Matter Interactions at Sub-Nuclear Density

Analogue to the effects of inhomogeneities for  $\nu$ -matter interactions discussed in the case of a first-order kaon condensate or quark matter transition is the case of coherent scattering of neutrinos from closely-spaced nuclei at sub-nuclear densities. The sizes and separations of nuclei are similar to those of the droplets discussed for the kaon and quark situations, so the range of neutrino energies most affected will be similar. These will be important in reshaping the  $\nu$  spectrum from PNSs, and are of potential importance in the supernova mechanism itself due to the large energy dependence of  $\nu$ -matter cross sections behind the shock.

In addition to these, several topics of interest from an astrophysical perspective include:

### Improvements in PNS Simulations

These include a) an adequate treatment of convection coupled with neutrino transport appear to be necessary based upon large regions that are potentially convectively unstable; b) the consideration of other softening components in dense matter that might produce effects dissimilar to those found when considering hyperons and kaons, i.e., quarks; c) improved transport calculations with many energy groups, especially in the transparent regime; d) a self-consistent



treatment of accretion, which is known to significantly contribute to the early  $\nu$  emission. The latter two items necessitate the coupling of a multi-group transport scheme with a hydrodynamical code of the type generally used for supernova simulations.

### Determination of the Neutron Skin of Neutron-rich Nuclei

The Jefferson Lab experiment [109] (PREX) is anticipated to yield accurate measurements of the neutron-skin thickness of  $^{208}\text{Pb}$ . This quantity, from a theoretical viewpoint, is the volume integral of the inverse of the symmetry energy throughout a nucleus, and represents how the nuclear symmetry energy is split between volume and surface contributions. Not coincidentally, the density dependence of the symmetry energy is also implicated in the predicted neutron star radius [5].

### Determination of the Radius of a Neutron Star

The best prospect for measuring a neutron star's radius may be the nearby object RX J185635-3754. Parallax information [129] indicates its distance to be about 60 pc. In addition, it may be possible to identify spectral lines with the Chandra and XMM X-ray facilities that would not only yield the gravitational redshift, but would identify the atmospheric composition. Not only would this additional information reduce the uncertainty in the deduced value of  $R_\infty$ , but, *both* the mass and radius for this object might thereby be estimated. It is also possible that an estimate of the surface gravity of the star can be found from further comparisons of observations with atmospheric modelling, and this would provide a further check on the mass and radius.

### Acknowledgements

Research support from NSF grant INT-9802680 (for MP and JML) and DOE grants FG02-88ER-40388 (for MP and AS) and FG02-87ER40317 (for JML and JAP) and FG06-90ER40561 (for SR) is gratefully acknowledged. It is a pleasure to acknowledge collaborations with George Bertsch, Greg Carter, Paul Ellis, Juan Miralles, and Dany Page who have contributed significantly to the material presented in this article.

### References

1. A. Burrows, J.M. Lattimer: *Astrophys. J.* **307**, 178 (1986)
2. A. Burrows: *Ann. Rev. Nucl. Sci.* **40**, 181 (1990)
3. A. Burrows: *Astrophys. J.* **334**, 891 (1988)
4. M. Prakash, I. Bombaci, Manju Prakash, P.J. Ellis, J.M. Lattimer, R. Knorren: *Phys. Rep.* **280**, 1 (1997) P.J. Ellis, J.M. Lattimer, M. Prakash: *Comm. Nucl. Part. Phys.* **22**, 63 (1996)

5. J.M. Lattimer, M. Prakash: *Astrophys. J. in press* (2000)
6. *Next Generation Nucleon Decay and Neutrino Dectector*, ed. by N. Diwan, C.K. Jung (AIP, New York 2000)
7. J.M. Lattimer, K.A. van Riper, M. Prakash, Manju Prakash: *Astrophys. J.* **425**, 802 (1994)
8. R.W. Lindquist: *Ann. Phys.* **37**, 478 (1966)
9. K.S. Thorne: *Mon. Not. R. Astron. Soc.* **194**, 439 (1981)
10. J.A. Pons, S. Reddy, M. Prakash, J.M. Lattimer, J.A. Miralles: *Astrophys. J.* **513**, 780 (1999)
11. A. Akmal, V.R. Pandharipande: *Phys. Rev. C* **56**, 2261 (1997)
12. B.D. Serot, J.D. Walecka: In *Advances in Nuclear Physics* Vol. 16, ed. by J.W. Negele, E. Vogt, (Plenum, New York 1986) p. 1
13. N.K. Glendenning, S. Moszkowski: *Phys. Rev. Lett.* **67**, 2414 (1991)
14. J.A. Pons, S. Reddy, P.J. Ellis, M. Prakash, J.M. Lattimer: *Phys. Rev. C* **62** 035803 (2000)
15. N.K. Glendenning, J. Schaffner-Bielich: *Phys. Rev. C* **60** 025803 (1999)
16. J.W. Gibbs: *Tran. Conn. Acad.* **III**, 108 (1876)
17. E. Friedman, A. Gal, C.J. Batty: *Nucl. Phys. A* **579**, 578 (1994)
18. E. Friedman, A. Gal, J. Mares, A. Cieply: *Phys. Rev. C* **60**, 024314 (1999)
19. T. Waas, W. Weise: *Nucl. Phys. A* **625**, 287 (1997)
20. A. Ramos, E. Oset: *Nucl. Phys. A* **671**, 481 (2000)
21. A. Baca, C. Garcia-Recio, J. Nieves: *Nucl. Phys. A* **673**, 335 (2000)
22. A.W. Steiner, M. Prakash, J.M. Lattimer: *Phys. Lett. B* **486** 239 (2000)
23. Manju Prakash, E. Baron, M. Prakash: *Phys. Lett. B*, **243**, 175 (1990)
24. Y. Nambu, G. Jona-Lasinio: *Phys. Rev.* **122**, 345 (1961)
25. G. 't Hooft: *Phys. Rep.* **142**, 357 (1986)
26. P. Rehberg, S.P. Klevansky, J. Hüfner: *Phys. Rev. C* **53**, 410 (1996)
27. T. Kunihiro: *Phys. Lett. B* **219**, 363 (1989)
28. T. Hatsuda, T. Kunihiro: *Phys. Rep.* **247**, 221 (1994)
29. M. Buballa, M. Oertel: *Phys. Lett. B* **457**, 261 (1999)
30. H. Müller, B.D. Serot: *Nucl. Phys. A* **606** (1996) 508
31. S. Reddy, G.F. Bertsch, M. Prakash: *Phys. Lett. B* **475**, 1 (2000)
32. N.K. Glendenning: *Phys. Rev. D* **46**, 1274 (1992)
33. J.M. Lattimer, D.G. Ravenhall: *Astrophys. J.* **223**, 314 (1978)
34. N.K. Glendenning, J. Schaffner-Bielich: *Phys. Rev. Lett.* **81**, 4564 (1998)
35. M. Christiansen, N.K. Glendenning, J. Schaffner-Bielich: *Phys. Rev. C* **62**, 025804 (2000) T. Norsen, S. Reddy: *nucl-th/0010075* (2000)
36. N.K. Glendenning, S. Pei: *Phys. Rev. C* **52**, 2250 (1995)
37. M. Prakash, J.R. Cooke, J.M. Lattimer: *Phys. Rev. D* **52**, 661 (1995)
38. S.W. Bruenn: *Astrophys. J. Supp.* **58**, 771 (1985)
39. A. Mezzacappa, S.W. Bruenn: *Astrophys. J.* **405**, 637 (1993)
40. J.R. Wilson, R.W. Mayle: In *The Nuclear Equation of State* Part A, ed. W. Greiner, H. Stöcker (Plenum, New York 1989) p. 731
41. H. Suzuki, K. Sato: In *The Structure and Evolution of Neutron Stars*, ed. D. Pines, R. Tamagaki, S. Tsuruta (Addison-Wesley, New York 1992) p. 276
42. W. Keil, H.T. Janka: *Astron. & Astrophys.* **296**, 145 (1995)
43. S. Reddy, J. Pons, M. Prakash, M., J.M. Lattimer: In *Stellar Evolution, Stellar Explosions and Galactic Chemical Evolution*, ed. T. Mezzacappa (IOP Publishing, Bristol 1997) p. 585
44. S. Reddy, M. Prakash: *Astrophys. J.* **423**, 689 (1997)

45. M. Prakash, S. Reddy: In *Nuclear Astrophysics*, ed. M. Buballa, W. Nörenberg, J. Wambach, A. Wirzba (GSI: Darmstadt 1997), p. 187
46. S. Reddy, M. Prakash, J.M. Lattimer: Phys. Rev. D **58**, 013009 (1998)
47. S. Reddy, M. Prakash, J.M. Lattimer, J.A. Pons: Phys. Rev. C **59**, 2888 (1999)
48. A. Burrows, R.F. Sawyer: Phys. Rev. C **58**, 554 (1998)
49. A. Burrows, R.F. Sawyer: Phys. Rev. C **59**, 510 (1999)
50. R.F. Sawyer: Phys. Rev. D **11**, 2740 (1975)
51. R.F. Sawyer: Phys. Rev. C **40**, 865 (1989)
52. N. Iwamoto, C.J. Pethick: Phys. Rev. D **25**, 313 (1982)
53. C.J. Horowitz, K. Wehrberger: Nucl. Phys. A **531**, 665 (1991) Phys. Rev. Lett. **66**, 272 (1991) Phys. Lett. B **226**, 236 (1992)
54. G. Raffelt, D. Seckel: Phys. Rev. D **52**, 1780 (1995)
55. G. Sigl: Phys. Rev. Lett **76**, 2625 (1996)
56. A.L. Fetter, J.D. Walecka: In *Quantum Theory of Many Particle Systems* (McGraw-Hill, New York 1971)
57. S. Doniach, E.H. Sondheimer: In *Green's Functions for Solid State Physicists* (The Benjamin/Cummings Publishing Company, Inc., Reading 1974)
58. J.M. Lattimer, C.J. Pethick, M. Prakash, P. Haensel: Phys. Rev. Lett. **66**, 2701 (1991)
59. C.J. Horowitz: Phys. Rev. D **55**, 4577 (1997)
60. N. Iwamoto, C.J. Pethick: Phys. Rev. D **25**, 313 (1982)
61. B.C. Barrois: Nucl. Phys. B **129**, 390 (1977) S.C. Frautschi: In *Workshop on Hadronic Matter at Extreme Energy Density* (Erice, Italy 1978)
62. M. Alford, K. Rajagopal, F. Wilczek: Phys. Lett. B **422**, 247 (1998) Nucl. Phys. B **357**, 443 (1999) *ibid.* **558**, 219 (1999) R. Rapp, T. Schäffer, E.V. Shuryak, M. Velkovsky: Phys. Rev. Lett. **81**, 53 (1998) Ann. Phys. **280**, 35 (2000)
63. D. Bailin, A. Love: Phys. Rept. **107**, 325 (1984)
64. G. W. Carter, S. Reddy: Phys. Rev. D **62** 103002 (2000)
65. J. Bardeen, L.N. Cooper, J.R. Schrieffer: Phys. Rev. **108**, 1175 (1957)
66. R.D. Pisarski, D.H. Rischke: Phys. Rev. D **61**, 051501 (2000)
67. R.D. Pisarski, D.H. Rischke: Phys. Rev. D **60**, 094013 (1999)
68. A. Burrows, B. Fryxell: Astrophys. J. Lett. **413**, L33 (1993)
69. M. Herant, W. Benz, J. Hicks, C. Fryer, S.A. Colgate: Astrophys. J. **425**, 339 (1994)
70. W. Keil, T.H. Janka, E. Müller: Astrophys. J. Lett. **473**, L111 (1995)
71. A. Mezzacappa, A.C. Calder, S.W. Bruenn, J.M. Blondin, M.W. Guidry, M.R. Strayer, A.S. Umar: Astrophys. J. **495**, 911 (1998)
72. J.A. Miralles, J.A. Pons, V.A. Urpin: Astrophys. J. **543**, 1001 (2000)
73. J.A. Pons, J.A. Miralles, M. Prakash, J.M. Lattimer: Astrophys. J. (2000) submitted; astro-ph/0008389
74. S. Tsuruta: Phys. Rep. **292**, 1 (1998) D. Page: in *The Many Faces of Neutron Stars*, ed. by R. Bucheri, J. van Paradijs, M.A. Alpar (Kluwer Academic Publishers, Dordrecht, 1998) p. 539
75. D. Page, J.H. Applegate: Astrophys. J. **394**, L17 (1992)
76. The relation between  $T_e$  and  $T$  is increased by about 50% if H or He dominates the atmosphere's composition. Our qualitative results concerning superfluidity, however, will be unaffected by the atmospheric composition.
77. M. Prakash, Manju Prakash, J.M. Lattimer, C.J. Pethick: Astrophys. J. **390**, L77 (1992)

78. C.J. Pethick: *Rev. Mod. Phys.* **64**, 1133 (1992) M. Prakash: *Phys. Rep.* **242**, 297 (1994) B. Friman, O.V. Maxwell: *Astrophys. J.* **232**, 541 (1979) N. Iwamoto: *Phys. Rev. Lett.* **44**, 1637 (1980)
79. M. Baldo, O. Elgaroy, L. Engvik, M. Hjorth-Jensen, H.-J. Schulze: *Phys. Rev. C* **58**, 1921 (1998)
80. S. Balberg, N. Barnea: *Phys. Rev. C* **57**, 409 (1997)
81. D.T. Son: *Phys. Rev. D* **59**, 094019 (1999) R. Pisarski, D. Rischke: *Phys. Rev. D* **61**, 051501 (2000) *ibid.* **61**, 074017 (2000) J. Berges, K. Rajagopal: *Nucl. Phys. B* **538**, 215 (1999) M. Alford, J. Berges, K. Rajagopal: *Phys. Rev. D* **D60**, 074014 (1999) T. Schäffer: *Nucl. Phys. A* **642**, 45 (1998) T. Schäffer, F. Wilczek: *Phys. Rev. Lett.* **82**, 3956 (1999) *Phys. Rev. D* **60**, 074014 (1999) G.W. Carter, D. Diakonov: *Phys. Rev. D* **60**, 16004 (1999)
82. P.F. Bedaque: hep-ph/9910247
83. D. Blaschke, T. Klahn, D.N. Voskresensky: *Astrophys. J.* **533**, 406 (2000)
84. D. Page, M. Prakash, J.M. Lattimer, A.W. Steiner: *Phys. Rev. Lett.* **85**, 2048 (2000)
85. K.P. Levenfish, D.G. Yakovlev: *Astronomy Rep.* **38**, 247 (1994) *Astronomy Lett.* **20**, 43 (1994) *Astronomy Lett.* **22**, 49 (1996)
86. E. Flowers, M. Ruderman, P. Sutherland: *Astrophys. J.* **205**, 541 (1976)
87. J. Zimanyi, S.A. Moszkowski: *Phys. Rev. C* **42**, 416 (1990)
88. T. Alm, G. Röpke, A. Sedrakian, F. Weber: *Nucl. Phys. A* **604**, 491 (1996)
89. D. Page: *Astrophys. J. Lett.* **479**, L43 (1997)
90. A. Akmal, V.R. Pandharipande, D.G. Ravenhall: *Phys. Rev. C* **58**, 1804 (1998)
91. D. Page: in *Neutron Stars and Pulsars: Thirty Years after the Discovery*, ed. by N. Shibazaki, et al. (Universal Academy Press, Tokyo 1998) p. 183
92. C. Schaab, S. Balberg, J. Schaffner-Bielich: *Astrophys. J. Lett.* **504**, L99 (1998)
93. J.M. Lattimer, M. Prakash, D. Masak, A. Yahil: *Astrophys. J.* **355** (1990) 241
94. B. Link, R.I. Epstein, J.M. Lattimer: *Phys. Rev. Lett.* **83** 3362 (1999)
95. M. Prakash, T.L. Ainsworth, J.M. Lattimer: *Phys. Rev. Lett.* **61** 2518 (1988)
96. B. Friedman, V.R. Pandharipande: *Nucl. Phys. A* **361** 502 (1981)
97. V.R. Pandharipande, R.A. Smith: *Nucl. Phys. A* **237** 507 (1975)
98. R.B. Wiringa, V. Fiks, A. Fabrocine: *Phys. Rev. C* **38** 1010 (1988)
99. H. Mütter, M. Prakash, T.L. Ainsworth: *Phys. Lett.* **199** 469 (1987)
100. L. Engvik, M. Hjorth-Jensen, E. Osnes, G. Bao, E. Østgaard: *Phys. Rev. Lett.* **73** 2650 (1994)
101. E. Witten: *Phys. Rev.* **D30** 272 (1984)
102. E. Fahri, R. Jaffe: *Phys. Rev.* **D30** 2379 (1984)
103. P. Haensel, J.L. Zdunik, R. Schaefer: *Astron. & Astrophys.* **217** 137 (1986)
104. C. Alcock, A. Olinto: *Ann. Rev. Nucl. Sci.* **38** 161 (1988)
105. Manju Prakash, E. Baron, M. Prakash: *Phys. Lett. B* **243** 175 (1990)
106. C.E. Rhoades, R. Ruffini: *Phys. Rev. Lett.* **32** 324 (1974)
107. N.K. Glendenning, F. Weber: *Astrophys. J.* **400** 672 (1992)
108. J.M. Lattimer, M. Prakash: *to be published*
109. C.J. Horowitz, S.J. Pollock, P.A. Souder, R. Michaels: nucl-th/9912038
110. R.C. Tolman: *Phys. Rev.* **55** 364 (1939)
111. H.A. Buchdahl: *Astrophys. J.* **147** 310 (1967)
112. D.G. Ravenhall, C.J. Pethick: *Astrophys. J.* **424** 846 (1994)
113. N.K. Glendenning: *Phys. Rev. D* **46** 4161 (1992)
114. J.M. Lattimer, A. Yahil: *Astrophys. J.* **340** 426 (1989)
115. L. Lindblom: *Astrophys. J.* **398** 569 (1992)

116. B. Friman, O. Maxwell: *Astrophys. J.* 232, 541 (1979)
117. R.F. Sawyer, A. Soni: *Astrophys. J.* **230**, 859 (1979)
118. P. Haensel, A.J. Jerzak: *Astron. & Astrophys.* **179**, 127 (1987)
119. D.H. Wilkinson: *Phys. Rev. C* **7**, 930 (1973)
120. M. Rho: *Nucl. Phys. A* **231**, 493 (1974)
121. G.E. Brown, M. Rho: *Phys. Rev. Lett.* **66**, 2720 (1991)
122. G. Carter, P.J. Ellis, S. Rudaz: *Nucl. Phys. A* **603**, 367 (1996)
123. S. Hannestad, G. Raffelt: *Astrophys. J.* **507**, 339 (1998)
124. J.A. Pons, J.A. Miralles, J.-M. Ibañez: *Astron. & Astrophys. Supp.* **129**, 343 (1998)
125. R.F. Sawyer, A. Soni: *Phys. Rev. Lett.* **38**, 1383 (1977)
126. R.F. Sawyer, A. Soni: *Phys. Rev. C* **18**, 898 (1978)
127. M. Ericson: *Nucl. Phys. A* **518**, 116 (1990)
128. R.F. Sawyer: *Phys. Rev. Lett.* **73**, 3363 (1994)
129. F.M. Walter: *Astrophys. J. in press* (2001)